

Contents lists available at ScienceDirect

# Petroleum Science

journal homepage: www.keaipublishing.com/en/journals/petroleum-science



# Original Paper

# Elastic impedance inversion for stress indicator in weakly orthorhombic media



Guang-Zhi Zhang <sup>a</sup>, Rui Yang <sup>a, \*</sup>, Lin Li <sup>a</sup>, You Zhou <sup>a</sup>, Huai-Zhen Chen <sup>b, c</sup>

- <sup>a</sup> School of Geosciences, China University of Petroleum (East China), Qingdao, Shangdong, 266580, China
- <sup>b</sup> School of Ocean and Earth Science, Tongji University, Shanghai, 200092, China
- <sup>c</sup> Department of Geoscience, University of Calgary, Calgary, Alberta, T2N 1N4, Canada

#### ARTICLE INFO

#### Article history: Received 4 May 2021 Accepted 7 March 2022 Available online 28 March 2022

Edited by Jie Hao

Keywords: Shale reservoir Stress Anisotropy Seismic inversion

### ABSTRACT

Hydraulic fracturing is a crucial technology for improving permeability and production of shale reservoirs. The precise estimation of the stress distribution has a significant guidance for optimizing the placement of hydraulic fracturing. Assuming that the shale gas reservoir is a weakly anisotropic medium with orthorhombic symmetry, a new stress indicator parameterized by rock mechanical parameters and fracture parameters is firstly presented to predict the differential horizontal stress ratio in shale gas reservoirs. Then, we derive a novel simplified P-to-P reflection coefficient and a logarithmic normalized elastic impedance (EI) as a function of Young's modulus, Poisson's ratio, Thomsen's WA parameter  $\delta_b$  and normal excess compliance Z<sub>N</sub>. Next, we adopt azimuthal EI inversion in a Bayesian framework to estimate rock mechanics parameters and fracture parameters directly on a fractured shale gas field seismic data. Finally, the stress indicator is determined by utilizing four inverted parameters. Synthetic examples demonstrate that the proposed approach produces stable parameter estimates even with moderate noise, verifying the feasibility and effectiveness of the method. Test on a field data set illustrates that the inversion results can be reasonably estimated, and the stress indicator derived by the inversion accords with the geomechanics result. Compared with the previous method, the new stress indicator has a higher capability to describe stress characteristics in the shale reservoir. We conclude that this stress evaluation procedure can provide reliable guidance for well location deployment and hydraulic fracturing reformation.

© 2022 The Authors. Publishing services by Elsevier B.V. on behalf of KeAi Communications Co. Ltd. This is an open access article under the CC BY-NC-ND license (http://creativecommons.org/licenses/by-nc-nd/4.0/).

# 1. Introduction

Stress prediction is one of the crucial technologies for hydraulic fracturing and well location deployment in shale reservoirs. Crampin (2001, 2006) utilized seismic shear-waves to indicate the direction of the stress based on the shear-wave splitting phenomenon. Warpinski and Smith (1989) described the rock mechanics and fracture geometry and proposed that the stress is important to hydraulic fracturing. Price and Cosgrove (1990) deduced a theoretical foundation for using curvature to estimate the stress. Iverson (1995) expanded in-situ horizontal stress formulas into anisotropic rocks and improved the accuracy of stress prediction. Sayers (2004) and Macbeth et al. (2012) used time-lapse seismic method to

predict the stress. Starr (2011) used seismic data to estimate the closure stress gradient. Sena et al. (2011) combined well-log information and prestack seismic data to estimate geomechanical properties and in-situ principal stresses. Gray et al. (2010, 2012) considered anisotropic characteristics of subsurface media and proposed the differential horizontal stress ratio (DHSR) to evaluate the stress property of unconventional reservoirs. Brew (2012) used anisotropy theory to identify the location and magnitude of regional stress and illustrated that there is a certain correlation between stress and azimuthal seismic data, but the quantitative relationship is unclear. Zhang et al. (2015) established a petrophysics model based on the prior information to obtain the elastic stiffness matrix of fractured anisotropic media and described the stress distribution of unconventional reservoirs. Ma et al. (2017, 2018) derived a new stress indicator expressed by shear-wave velocity and fracture parameters for the induced fracture orthorhombic model and used azimuthal pre-stack seismic data to

E-mail address: yangrui199711@gmail.com (R. Yang).

<sup>\*</sup> Corresponding author.

estimate DHSR. Du et al. (2021) modified the DHSR equation for evaluating the stress property of the equivalent HTI media for gasbearing shale reservoirs. Chen et al. (2020) present a nonlinear inversion workflow for a stress-sensitive parameter based on the CP model.

Young's modulus and Poisson's ratio, as a kind of geomechanical parameters, play a crucial role in predicting in-situ stresses acting on shale reservoirs (Sena et al., 2011). Iverson (1995) shows that Young's modulus and Poisson's ratio can be used to estimate the insitu stress state of anisotropic rocks. As the concept of rock brittleness, Young's modulus reflects the rocks' ability to maintain a fracture under stress and Poisson's ratio reflects the rocks' ability to fail once the rock fractures. Brittle shale is more likely to develop fractures and respond to hydraulic fracturing treatments (Rickman et al., 2008). Gray et al. (2012) illustrated that DHSR, as the differential ratio of the maximum and minimum horizontal stresses calculated from Young's modulus and Poisson's ratio, is a very important parameter in determining how these rocks will fracture under the stresses induced by hydraulic fracturing. On the other hand, fractures are important storage zones of hydrocarbon in shale reservoirs (Bachrach et al., 2009; Pan et al., 2018a). The actual shale reservoir is usually assumed to a weakly orthorhombic media constructed by a suite of parallel vertical fractures embedded in a vertical transversely isotropic background. Thomsen's weakly anisotropic parameters and fracture weaknesses play a significant role in fractured media, but it is difficult to derive an analytical P-to-P reflection coefficient expression due to the complexity of seismic wave propagation. Much researches have been discussed in simplifying the reflection coefficient expression of orthorhombic media (Rüger, 2002; Pšenčík and Martins, 2001; Bachrach et al., 2009; 2015). Bakulin et al. (2002) integrated the relations between Thomsen's weakly anisotropic parameters and fracture weaknesses to estimate fracture parameters of orthorhombic models. Pan et al. (2018b) combined the weak anisotropic assumption and scattering theory to derive linearized reflection coefficient expressed by moduli parameters, density, and anisotropic parameters in an orthorhombic medium. In the last decades, elastic impedance inversion method has been widely implemented in seismic inversion due to its practicability (Connolly, 1999; Mallick, 2001; Martins, 2006; Yin et al., 2013).

Under the assumptions that the shale gas reservoir is a weakly orthorhombic medium constituted by horizontal layered strata with vertical fractures, we first construct a new orthorhombic differential horizontal stress ratio (ODHSR<sub>new</sub>) utilizing Young's modulus, Poisson's ratio, and fracture parameters as the stress indicator. Next, we deduce a simplified P-to-P reflection coefficient and an azimuthal elastic impedance expression in terms of Young's modulus, Poisson's ratio, Thomsen's WA parameter, and normal excess compliance. Finally, we estimate rock mechanics parameters and fracture parameters directly by using Bayesian EI inversion approach and calculate the new stress indicator ODHSR<sub>new</sub>. Compared with previous azimuthal EI inversion, the proposed approach avoids accumulation errors caused by the indirect estimation of Young's modulus and Poisson's ratio and improves the stability of inversion process since reducing the number of estimated parameters. The test results are consistent with geology interpretation in the study field and demonstrate that the proposed approach has the potential of precise stress prediction.

### 2. Theory and method

### 2.1. Stress indicator for weakly orthorhombic media

Schoenberg and Helbig (1997) presented that a single suite of parallel vertical fractures embedded in a VTI medium can be taken

as an orthorhombic medium (Fig. 1), and the effective elastic compliance tensor  $\mathbf{S_{OA}}$  of the orthorhombic medium is expressed as (Rüger, 2002)

$$\mathbf{S_{OA}} = \mathbf{C_{OA}^{-1}} = \begin{bmatrix} s_{11} & s_{12} & s_{13} & 0 & 0 & 0 \\ s_{12} & s_{22} & s_{23} & 0 & 0 & 0 \\ s_{13} & s_{23} & s_{33} & 0 & 0 & 0 \\ 0 & 0 & 0 & s_{44} & 0 & 0 \\ 0 & 0 & 0 & 0 & s_{55} & 0 \\ 0 & 0 & 0 & 0 & 0 & s_{66} \end{bmatrix}, \tag{1}$$

where, the compliance coefficients  $s_{ij}$  (i = 1-6, j = 1-6) in the matrix are related to rock mechanical parameters and fracture parameters (Pan et al., 2018a), which are given in detail in Appendix A.

Based on the constitutive equation of orthorhombic media and the general expression of Hooke's law, the relationship between the strain and the stress with the compliance matrix is expressed as

$$\begin{bmatrix} \varepsilon_{1} \\ \varepsilon_{2} \\ \varepsilon_{3} \\ \varepsilon_{4} \\ \varepsilon_{5} \\ \varepsilon_{6} \end{bmatrix} = \begin{bmatrix} s_{11} & s_{12} & s_{13} & 0 & 0 & 0 \\ s_{12} & s_{22} & s_{23} & 0 & 0 & 0 \\ s_{13} & s_{23} & s_{33} & 0 & 0 & 0 \\ 0 & 0 & 0 & s_{44} & 0 & 0 \\ 0 & 0 & 0 & 0 & s_{55} & 0 \\ 0 & 0 & 0 & 0 & 0 & s_{66} \end{bmatrix} \begin{bmatrix} \sigma_{1} \\ \sigma_{2} \\ \sigma_{3} \\ \sigma_{4} \\ \sigma_{5} \\ \sigma_{6} \end{bmatrix},$$
(2)

where,  $e_i$  (i = 1-6) represents the strain tensor of the orthorhombic medium, and  $\sigma_i$  (i = 1-6) represents the stress tensor of the orthorhombic medium.

Under the assumptions that one principal stress is vertical, the other two are horizontal, and the rock is bounded and cannot be moved, so the strains in all direction of the rock is zero (Gray et al., 2012).

$$\varepsilon_{\mathsf{X}} = \varepsilon_1 = \mathsf{S}_{11}\sigma_{\mathsf{X}} + \mathsf{S}_{12}\sigma_{\mathsf{V}} + \mathsf{S}_{13}\sigma_{\mathsf{Z}} = 0 \tag{3}$$

$$\varepsilon_{\mathbf{v}} = \varepsilon_2 = s_{12}\sigma_{\mathbf{v}} + s_{22}\sigma_{\mathbf{v}} + s_{23}\sigma_{\mathbf{z}} = 0 \tag{4}$$

where,  $\varepsilon_X$  and  $\varepsilon_Y$  represent the xz- and xy- plane stress tensors, respectively.  $\sigma_X$ ,  $\sigma_Y$  and  $\sigma_Z$  represent the xz- and xy- plane strain tensors, respectively.

Using the compliance coefficients  $s_{ij}$  expressed by Young's modulus, Poisson's ratio, and fracture parameters in Eq. (1) to reexpress Eqs. (3) and (4), we derive the minimum horizontal stress  $\sigma_x$  and the maximum horizontal stress  $\sigma_y$  in terms of rock mechanical parameters and fracture parameters as

$$\sigma_{x} = \sigma_{z} \frac{s_{12}s_{23} - s_{13}s_{22}}{s_{11}s_{22} - s_{12}^{2}} = \sigma_{z} \frac{\sigma - \frac{E\sigma(1-\sigma)}{(1+\sigma)(1-2\sigma)}Z_{N} + (1-\sigma)\delta_{b}}{1 - \sigma - \frac{E\sigma^{2}}{(1+\sigma)(1-2\sigma)}Z_{N}}$$
(5)

$$\sigma_{y} = \sigma_{z} \frac{s_{12}s_{13} - s_{11}s_{23}}{s_{11}s_{22} - s_{12}^{2}} = \sigma_{z} \frac{\sigma - \frac{E\sigma^{2}}{(1+\sigma)(1-2\sigma)}Z_{N} + (1-\sigma)\delta_{b}}{1 - \sigma - \frac{E\sigma^{2}}{(1+\sigma)(1-2\sigma)}Z_{N}},$$
 (6)

where  $\sigma_Z$  represents the vertical stress of weakly orthorhombic media, E and  $\sigma$  represent Young's modulus and Poisson's ratio of homogeneous isotropic media,  $\delta_b$  is the Thomsen's WA parameter of VTI background media, and  $Z_N$  is the normal excess compliance of aligned vertical fractures (Thomsen, 1986; Schoenberg and Helbig, 1997).

Hence, a new stress indicator for orthorhombic media, *ODHSR*<sub>new</sub>, which is parameterized by rock mechanics parameters and fracture parameters, is given by

$$\begin{split} \textit{ODHSR}_{new} &= \frac{\sigma_y - \sigma_x}{\sigma_y} \\ &= \frac{\textit{E}\sigma \textit{Z}_N (1 - 2\sigma)}{2\sigma^3 (\delta_b - 1) - \sigma^2 (\textit{EZ}_N + \delta_b + 1) + \sigma (1 - 2\delta_b) + \delta_b} \end{split}$$

fracture parameters which have crucial impacts in stress prediction of shale gas reservoirs to simplify Eq. (8).

For the isotropic section  $R_{PP}^{iso}(\theta)$ , referring to the approximate reflection coefficient formula derived by Zong et al. (2012), we use the relationship between the density and P-wave velocity of Gardner formula (Gardner et al., 1974) to eliminate the density term (Du et al., 2015), so the simplified expression is given by

$$R_{\text{PP}}^{\text{iso}}(\theta) = \left[ \frac{1}{2(n+2)} \sec^2 \theta + \frac{n}{2(n+2)} - 2g\sin^2 \theta \right] \frac{\Delta E}{E} + \left\{ 2g\sin^2 \theta \frac{1 - 2g}{3 - 4g} + \left[ \frac{1}{2(n+2)} \sec^2 \theta + \frac{n}{2(n+2)} \right] \right\} \frac{(2g-3)(2g-1)^2}{g(4g-3)} \frac{\Delta \sigma}{\sigma}$$
(11)

To avoid the error accumulation of indirect calculations and enhance the stability of inversion process, we next discuss a simplified four-term P-to-P reflection coefficient in terms of Young's modulus E, Poisson's ratio  $\sigma$ , Thomsen's WA parameter  $\delta_{\rm b}$ , and normal excess compliance  $Z_{\rm N}$  and then implement Bayesian elastic impedance (EI) inversion workflow to directly estimate unknown parameters.

# 2.2. Derivation of P-to-P reflection coefficient and azimuthal elastic impedance for a weakly orthorhombic medium

Based on the weakly anisotropic theory and scattering function, Pan et al. (2018a) proposed a P-to-P reflection coefficient of orthorhombic media expressed by P- and S-wave moduli, density, and five anisotropic parameters.

$$R_{\rm PP}(\theta,\varphi) = R_{\rm PP}^{\rm iso}(\theta) + \Delta R_{\rm PP}^{\rm ani}(\theta,\varphi) \tag{8}$$

where.

$$R_{\rm PP}^{\rm iso}(\theta) = \frac{\sec^2 \theta}{4} \frac{\Delta M}{M} - 2g\sin^2 \theta \frac{\Delta \mu}{\mu} + \frac{1}{2} \left( 1 - \frac{\sec^2 \theta}{2} \right) \frac{\Delta \rho}{\rho} \tag{9}$$

where,  $g=(1-2\overline{\sigma})/(2-2\overline{\sigma}),~\theta$  is the incidence angle,  $\varphi$  is the azimuthal angle,  $\overline{E}$  and  $\overline{\sigma}$  are the averages over the interface,  $\Delta E$ ,  $\Delta \sigma$ ,  $\Delta \delta_{\rm b}$ , and  $\Delta Z_{\rm N}$  are the corresponding contrasts, and the constant n represents the power exponent of P-wave velocity in Gardner formula, which is related to the rock characteristics of shale reservoirs. In this study, we set n=0.044.

For the anisotropic section  $\Delta R_{PP}^{ani}(\theta, \varphi)$ , in the case of a weakly anisotropic medium, we neglect the higher-order terms about  $\Delta \delta_{H}$ , and when fractured reservoirs are filled with gas, we can replace  $\Delta \delta_{T}$  with  $\Delta \delta_{N}$  (Bakulin et al., 2000)

$$\Delta \delta_{\rm T} = \frac{4g(1-g)}{3-2g} \Delta \delta_{\rm N}. \tag{12}$$

We use the relationship between the normal fracture compliance and the normal fracture weakness to yield (Schoenberg and Helbig, 1997)

$$\Delta \delta_{N} = \frac{\overline{E}(1-g)}{g(3-4g)} Z_{N} \tag{13}$$

Substituting Eq. (12) and Eq. (13) into Eq. (10), the anisotropic part  $\Delta R_{\rm pp}^{\rm ani}(\theta,\varphi)$  is given by

$$\begin{split} & \Delta R_{\text{PP}}^{\text{ani}}(\theta,\varphi) = \frac{\sin^2\theta \tan^2\theta}{2} \Delta \varepsilon_{\text{b}} + \frac{\sin^2\theta}{2} \Delta \delta_{\text{b}} - \frac{\sec^2\theta}{4} \Big[ 2\frac{\mu}{M} \Big( \sin^2\theta \sin^2\varphi + \cos^2\theta \Big) - 1 \Big]^2 \Delta \delta_{\text{N}} \\ & + \frac{\mu}{M} \sin^2\theta \cos^2\varphi \Delta \delta_{\text{T}} - \frac{\mu}{M} \sin^2\theta \tan^2\theta \sin^2\varphi \cos^2\varphi \Delta \delta_{\text{H}} \end{split} \tag{10}$$

where, E,  $\mu$ , and  $\rho$  represent P-wave modulus, S-wave modulus, and density of the isotropic background, respectively.  $\varepsilon_{\rm b}$  and  $\delta_{\rm b}$  are Thomsen's weakly anisotropic parameters of VTI background,  $\delta_{\rm N}$ ,  $\delta_{\rm T}$ , and  $\delta_{\rm H}$  are the normal fracture weakness, vertical fracture weakness and horizontal tangential fracture weakness, respectively. The sign  $\Delta$  represents the perturbation across the reflection interface.

However, the linearized P-to-P reflection coefficient proposed by Pan et al. (2018a) is complicated and difficult to invert all eight parameters accurately using observed seismic datasets. To solve this problem, we first select rock mechanics parameters and

$$\begin{split} \Delta R_{\text{PP}}^{\text{ani}}(\theta,\varphi) &= \frac{1}{2}\sin^2\theta\Delta\delta_{\text{b}} + \left\{ \\ &- \frac{1}{4}\sec^2\theta \left[ 2g \left( \sin^2\theta\sin^2\varphi + \cos^2\theta \right) - 1 \right]^2 \\ &+ \frac{4g^2(1-g)}{3-2g}\sin^2\theta\cos^2\varphi \right\} \frac{\bar{E}(1-g)}{g(3-4g)}\Delta Z_{\text{N}} \end{split}$$
 (14)

Combining Eq. (11) and Eq. (14), we obtain the simplified P-to-P reflection coefficient for a weakly orthorhombic medium as

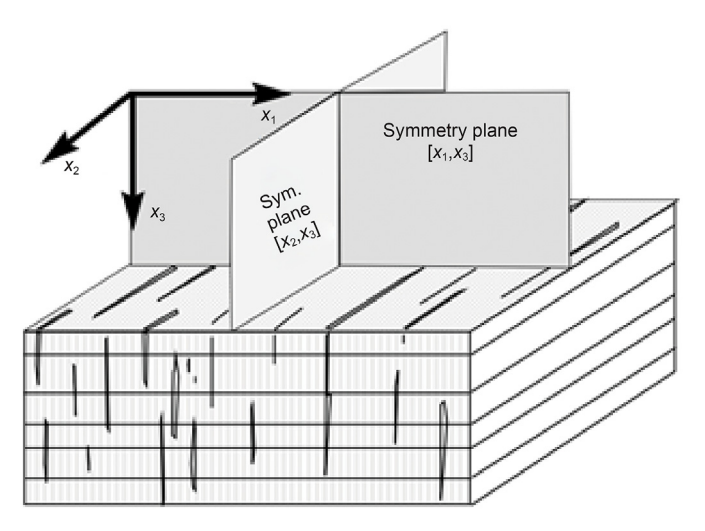


**Fig. 1.** An orthorhombic model combining thin horizontal layers and a set of parallel vertical cracks (Rüger, 2002).

Therefore, the seismic data containing large incidence angle information is necessary to estimate  $\Delta \sigma/\bar{\sigma}$  accurately.

Fig. 3c and d show that the effects of perturbations in Thomsen's WA parameter  $\delta_{\rm b}$  and the normal excess compliance  $Z_{\rm N}$  on the P-to-P reflection coefficient. We observe that reflection amplitudes in the range of small incidence angle almost have no perturbation with the variation of Thomsen's WA parameter  $\Delta\delta_{\rm b}$ , but it is responsive at the large incidence angle of approximately 40° (Fig. 3c). Meanwhile, the perturbations in  $\Delta Z_{\rm N}$  contribute to the reflection coefficient among the full range of incidence and azimuthal angles, especially it is sensitive over the middle incidence angle of 20° (Fig. 3d). Therefore, we need high-angle seismic data to estimate  $\delta_{\rm b}$  and  $Z_{\rm N}$  precisely.

Following Connolly (1999) and Martins (2006), we obtain the relationship between P-to-P reflection coefficient and azimuthal elastic impedance:

$$R_{\rm PP} \approx \frac{1}{2} \frac{\Delta EI}{\overline{FI}} \approx \frac{1}{2} \Delta \ln EI,$$
 (16)

$$\begin{split} R_{PP}(\theta,\varphi) &= \left[ \frac{1}{2(n+2)} sec^2 \theta + \frac{n}{2(n+2)} - 2g sin^2 \theta \right] \frac{\Delta E}{\overline{E}} \\ &+ \left\{ 2g sin^2 \theta \frac{1-2g}{3-4g} + \left[ \frac{1}{2(n+2)} sec^2 \theta + \frac{n}{2(n+2)} \right] \frac{(2g-3)(2g-1)^2}{g(4g-3)} \right\} \frac{\Delta \sigma}{\overline{\sigma}} \\ &+ \frac{1}{2} sin^2 \theta \Delta \delta_b + \frac{\overline{E}(1-g)}{(3-4g)} \left\{ -\frac{1}{4g} sec^2 \theta \left[ 2g \left( sin^2 \theta sin^2 \varphi + cos^2 \theta \right) - 1 \right]^2 + \frac{4g(1-g)}{3-2g} sin^2 \theta cos^2 \varphi \right\} \Delta Z_N \end{split}$$
 (15)

We use a two-layer model (in Table 1) to analyze the accuracy of the novel approximation in Eq. (15). Table 1 shows elastic parameters and fracture parameters of the isotropic and the orthorhombic medium. Fig. 2 display the comparison of the novel approximation (the curves in green), the approximation of Pan et al. (2018b) (the curves in red), and the exact equation of Zoeppritz and Erdbebenwellen (1919) (the curves in black) for azimuths of 0° and 90°. We observe that the novel approximate equation are in good agreement with exact Zoeppritz's equation when the incidence angle is less than 40°. Compared with the approximation of Pan et al. (2018b), the proposed novel equation is more accurate at large azimuthal angles.

To further analyze the sensitivity of the P-to-P reflection coefficient to model parameters, we use the model parameters given by the two-layer model (in Table 1) to calculate the reflection coefficients by using Eq. (15).

First, we illustrate the perturbations in Young's modulus E, Poisson's ratio  $\sigma$  that how they affect the reflection coefficient equation. Fig. 3a shows that the reflectivity of Young's modulus  $\Delta E/\overline{E}$  contributes to  $R_{\rm PP}$  over the whole range of incidence and azimuthal angles with a close weight, which means that  $\Delta E/\overline{E}$  can be inverted well. Fig. 3b shows that the reflectivity of Poisson's ratio  $\Delta \sigma/\overline{\sigma}$  also contributes to  $R_{\rm PP}$  over the whole range of incidence and azimuthal angles, but it is more responsive at the large angles.

**Table 1**Elastic and anisotropic parameters of the two-layer model.

Layers	$\alpha$ , km/s	$\beta$ , km/s	ho, g/cm <sup>3</sup>	$\delta_{\mathrm{b}}$	$\epsilon_{\mathrm{b}}$	$\delta_{ m N}$	$\delta_{\mathrm{T}}$	$\delta_{H}$
Isotropic OA	5.049 4.645	3.342 2.851	2.541 2.395	0.000 0.07		0.000	0.000 0.240	
UA	4.045	2.651	2.595	0.07	0.1	0.541	0.240	0.003

where,

$$\Delta E \overline{E} \approx \Delta \ln E \ \Delta \sigma \overline{\sigma} \approx \Delta \ln \sigma, \tag{17}$$

Combining Eqs. 15-17, we derive the perturbation in EI as

$$\begin{split} &\Delta lnEI = \left(\frac{1}{n+2}sec^2\theta + \frac{n}{n+2} - 4gsin^2\theta\right)\Delta lnE \\ &+ \left[4gsin^2\theta \frac{1-2g}{3-4g} + \left(\frac{1}{n+2}sec^2\theta + \frac{n}{n+2}\right)\frac{(2g-3)(2g-1)^2}{g(4g-3)}\right]\Delta ln\sigma \\ &+ sin^2\theta\Delta\delta_b + \frac{\overline{E}(1-g)}{(3-4g)}\left\{-\frac{1}{2g}sec^2\theta\left[2g\left(sin^2\theta sin^2\varphi + cos^2\theta\right) - 1\right]^2 \right. \\ &+ \frac{8g(1-g)}{3-2g}sin^2\theta cos^2\varphi\right\}\Delta Z_N \end{split}$$

Finally, we obtain the elastic impedance expression as

$$EI(\theta,\varphi) = EI_0 \left(\frac{E}{E_0}\right)^{a(\theta)} \left(\frac{\sigma}{\sigma_0}\right)^{b(\theta)} \exp[c(\theta)\delta_b + d(\theta,\varphi)Z_N]$$
 (19)

where,

$$a(\theta) = \frac{1}{n+2}\sec^2\theta + \frac{n}{n+2} - 4g\sin^2\theta,$$
 (20)

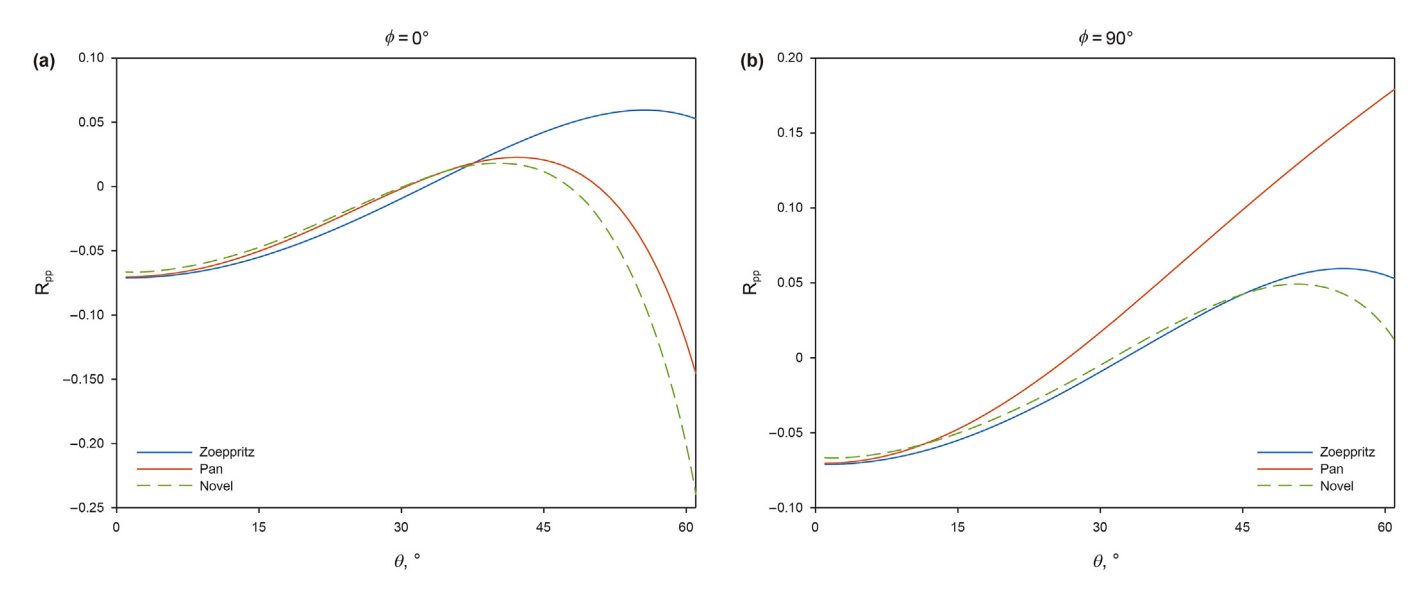


Fig. 2. Comparison of Zoeppritz's equation (the curves in black), Pan's approximation (the curves in red), and the novel approximation (the curves in green) for azimuths of 0° and 90°

$$b(\theta) = 4g\sin^2\theta \frac{1 - 2g}{3 - 4g} + \left(\frac{1}{n+2}\sec^2\theta + \frac{n}{n+2}\right) \frac{(2g-3)(2g-1)^2}{g(4g-3)},$$
 (21)

$$c(\theta) = \sin^2 \theta \tag{22}$$

the inversion for anisotropic El datasets using partially incidenceangle-stacked seismic data; and 2) the estimation of Young's modulus, Poisson's ratio, and anisotropic parameters from the inverted El datasets.

Analyzing the azimuthal anisotropic elastic impedance formula in Eq. (19), we observe that there is a nonlinear exponential relationship between rock mechanics parameters and anisotropic parameters and azimuthal elastic impedance. In the present study, we first express the logarithmic azimuthal EI as

$$d(\theta,\varphi) = \frac{\overline{E}(1-g)}{(3-4g)} \left\{ -\frac{1}{2g} \sec^2\theta \left[ 2g \left( \sin^2\theta \sin^2\varphi + \cos^2\theta \right) - 1 \right]^2 + \frac{8g(1-g)}{3-2g} \sin^2\theta \cos^2\varphi \right\}$$
 (23)

# 2.3. Bayesian El inversion for Young's modulus, Poisson's ratio, and orthorhombic anisotropic characteristic parameters

Bayesian EI inversion workflow is widely used to estimate elastic parameters (e.g., Young's modulus and Poisson's ratio) and fracture parameters (e.g., Thomsen parameters and fracture compliance), we accomplish it as a two-step process involving: 1)

$$\ln\left[\frac{EI(\theta,\varphi)}{EI_0}\right] = a(\theta)\ln\left(\frac{E}{E_0}\right) + b(\theta)\ln\left(\frac{\sigma}{\sigma_0}\right) + c(\theta)\delta_b + d(\theta,\varphi)Z_N. \tag{24}$$

In the case of m azimuthal angles and k incidence angles, Eq. (24) is expressed as

$$\begin{cases}
\ln\left[\frac{EI(\theta_{1},\varphi_{1})}{EI_{0}}\right] = a(\theta_{1})\ln\left(\frac{E}{E_{0}}\right) + b(\theta_{1})\ln\left(\frac{\sigma}{\sigma_{0}}\right) + c(\theta_{1})\delta_{b} + d(\theta_{1},\varphi_{1})Z_{N} \\
\vdots \\
\ln\left[\frac{EI(\theta_{k},\varphi_{1})}{EI_{0}}\right] = a(\theta_{k})\ln\left(\frac{E}{E_{0}}\right) + b(\theta_{k})\ln\left(\frac{\sigma}{\sigma_{0}}\right) + c(\theta_{k})\delta_{b} + d(\theta_{k},\varphi_{1})Z_{N} \\
\vdots \\
\ln\left[\frac{EI(\theta_{1},\varphi_{m})}{EI_{0}}\right] = a(\theta_{1})\ln\left(\frac{E}{E_{0}}\right) + b(\theta_{1})\ln\left(\frac{\sigma}{\sigma_{0}}\right) + c(\theta_{1})\delta_{b} + d(\theta_{1},\varphi_{m})Z_{N} \\
\vdots \\
\ln\left[\frac{EI(\theta_{k},\varphi_{m})}{EI_{0}}\right] = a(\theta_{k})\ln\left(\frac{E}{E_{0}}\right) + b(\theta_{k})\ln\left(\frac{\sigma}{\sigma_{0}}\right) + c(\theta_{k})\delta_{b} + d(\theta_{k},\varphi_{m})Z_{N}
\end{cases}$$
(25)

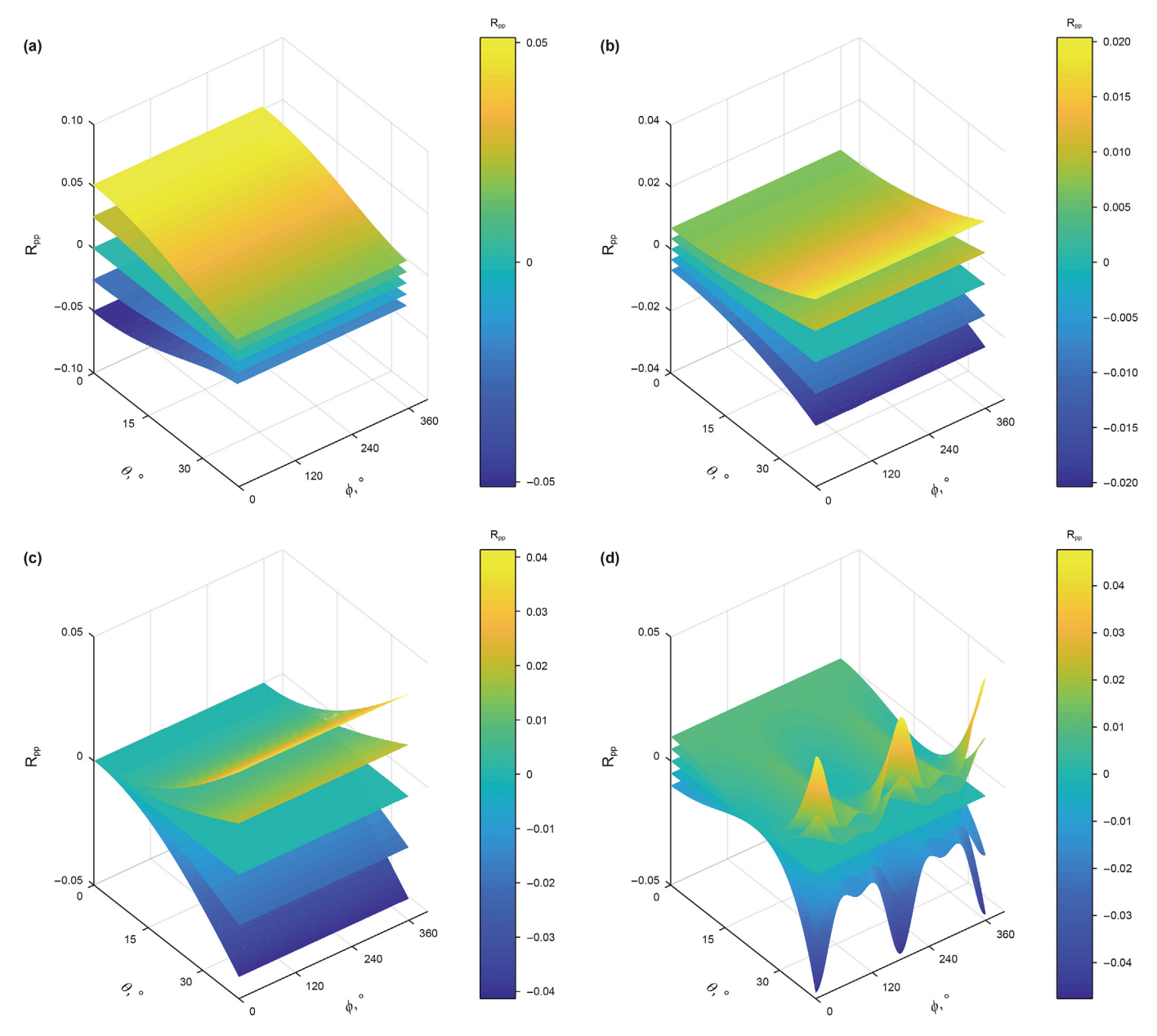


**Fig. 3.** Effects of perturbations in Young's modulus E, Poisson's ratio  $\sigma$ , Thomsen's WA parameter  $\delta_b$ , and the normal excess compliance  $Z_N$  on the reflection coefficient, where (a)  $\Delta E/\overline{E}$  variation from -0.2 to 0.2, (b)  $\Delta \sigma/\overline{\sigma}$  variation from -0.2 to 0.2, (c)  $\Delta \delta_b$  variation from -0.2 to 0.2, and (d)  $\Delta Z_N$  variation from -0.2 to 0.2. The interval of changes in model parameters is 0.1. The bottom sheets of (a)–(d) correspond to model parameter values of -0.2.

To solve Young's modulus E, Poisson's ratio  $\sigma$ , Thomsen's weakly anisotropic parameter  $\delta_{\rm b}$ , and the normal excess compliance  $Z_{\rm N}$ , Eq. (25) can be concisely given by

where,

$$\mathbf{d} = \begin{bmatrix} LEI(\theta_{1}, \phi_{1}) \\ \vdots \\ LEI(\theta_{k}, \phi_{1}) \\ \vdots \\ LEI(\theta_{1}, \phi_{m}) \\ \vdots \\ LEI(\theta_{k}, \phi_{m}) \end{bmatrix}_{kmJ \times 1}, \mathbf{m} = \begin{bmatrix} L_{E} \\ L_{\sigma} \\ \delta_{b} \\ Z_{N} \end{bmatrix}_{4J \times 1}, \mathbf{G} = \begin{bmatrix} A(\theta_{1}) & B(\theta_{1}) & C(\theta_{1}) & D(\theta_{1}, \phi_{1}) \\ \vdots & \vdots & \vdots & \vdots \\ A(\theta_{k}) & B(\theta_{k}) & C(\theta_{k}) & D(\theta_{k}, \phi_{1}) \\ \vdots & \vdots & \vdots & \vdots \\ A(\theta_{1}) & B(\theta_{1}) & C(\theta_{1}) & D(\theta_{1}, \phi_{m}) \\ \vdots & \vdots & \vdots & \vdots \\ A(\theta_{k}) & B(\theta_{k}) & C(\theta_{k}) & D(\theta_{k}, \phi_{m}) \end{bmatrix}_{kmJ \times 4J}$$
(26)

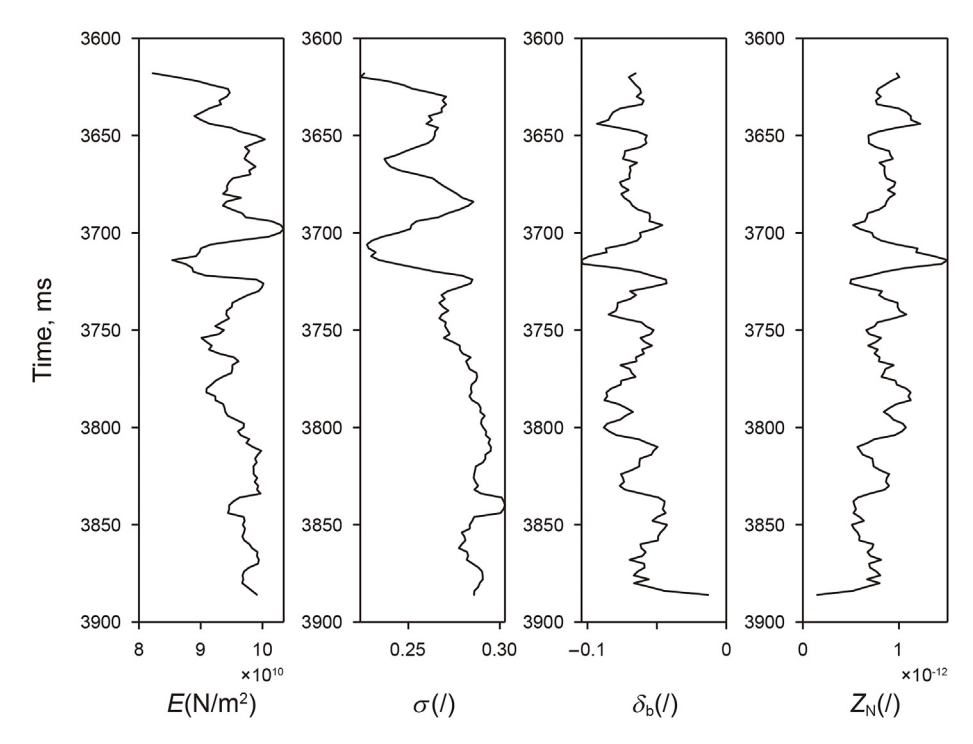


Fig. 4. The well-log data calculated by rock-physics model: Young's modulus E, Poisson's ratio  $\sigma$ , Thomsen's WA parameter  $\delta_{\rm b}$ , and the normal excess compliance  $Z_{\rm N}$ .

and where, 
$$LEI = \left[\ln\left(\frac{EI}{EI_0}\right)^1, \cdots, \ln\left(\frac{EI}{EI_0}\right)^J\right]_{J\times 1}^T$$
,  $L_E = \left[\ln E^1, \cdots, \ln E^J\right]_{J\times 1}^T$ ,  $L_{\sigma} = \left[\ln \sigma^1, \cdots, \ln \sigma^J\right]_{J\times 1}^T$ ,  $\delta_b = \left[\delta_b^{\ 1}, \cdots, \delta_b^{\ J}\right]_{J\times 1}^T$ ,  $Z_N = \left[Z_N^{\ 1}, \cdots, Z_N^{\ J}\right]_{J\times 1}^T$ ,

$$\begin{split} A(\theta_i) &= diag \Big[ a^1(\theta_i),...,a^J(\theta_i) \Big]_{J\times J}, \ B(\theta_i) \\ &= diag \Big[ b^1(\theta_i),...,b^J(\theta_i) \Big]_{J\times J}, \ C(\theta_i) \\ &= diag \Big[ c^1(\theta_i),...,c^J(\theta_i) \Big]_{J\times J}, \ D(\theta_i) \\ &= diag \Big[ d^1(\theta_i,\varphi_j),...,d^J(\theta_i,\varphi_j) \Big]_{J\times J}. \end{split}$$

in which  $\theta_i$  and  $\varphi_j$  are the *i*th incidence angle and the *j*th azimuth, respectively. The superscript and subscript *J* represents the number of interfaces, and the *diag* means the diagonal matrix.

To solve the problem that model parameters have a general correlation, we need to do the decorrelation process, which is given in detail in Appendix B. Following the prestack EI inversion method and Bayesian theory introduced by Zong et al. (2012), we use Cauchy distribution as the prior probability model  $p(\mathbf{m}')$ , and assume that the seismic data noise conforms to the Gaussian distribution and use it as the likelihood function  $p(\mathbf{d}|\mathbf{m}')$ . Hence, the posterior probability distribution function of the model parameter is consisted of the prior probability model and the likelihood function as

$$p(\mathbf{m}', \sigma_{\mathbf{n}}|\mathbf{d}) \propto p(\mathbf{m}')p(\mathbf{d}|\mathbf{m}') = \prod_{i=1}^{4J} \left[ \frac{1}{1 + \mathbf{m}_{i}'^{2} / \sigma_{\mathbf{m}'}^{2}} \right]$$

$$\cdot \exp \left[ -\frac{(\mathbf{G}'\mathbf{m}' - \mathbf{d})^{T} (\mathbf{G}'\mathbf{m}' - \mathbf{d})}{2\sigma_{\mathbf{n}}^{2}} \right],$$
(27)

where  $\sigma_{\rm n}^2$  represents the noise variance, and  $\sigma_{{\bf m}'}^2$  represents the

variance of model parameter vector.

To enhance the stability of the inversion and maximize the posterior probability distribution, we next add the low-frequency constraints to the objective function, so the objective function is expressed as

$$F(\mathbf{m}') = (\mathbf{d} - \mathbf{G}'\mathbf{m}')^{T}(\mathbf{d} - \mathbf{G}'\mathbf{m}') + 2\sigma_{n}^{2} \sum_{i=1}^{M} \ln\left(1 + \mathbf{m}'_{i}^{2} / \sigma_{\mathbf{m}'}^{2}\right) + \Lambda$$
(28)

where,

$$\begin{split} \boldsymbol{\varLambda} &= \lambda_{E} \big( \eta_{E} - P\boldsymbol{L}_{E}^{'} \big)^{T} \big( \eta_{E} - P\boldsymbol{L}_{E}^{'} \big) + \lambda_{\sigma} \big( \eta_{\sigma} - P\boldsymbol{L}_{\sigma}^{'} \big)^{T} \big( \eta_{\sigma} - P\boldsymbol{L}_{\sigma}^{'} \big) \\ &+ \lambda_{\delta_{b}} \Big( \eta_{\delta_{b}} - P\boldsymbol{L}_{\delta_{b}}^{'} \Big)^{T} \Big( \eta_{\delta_{b}} - P\boldsymbol{L}_{\delta_{b}}^{'} \Big) + \lambda_{Z_{N}} \Big( \eta_{Z_{N}} - P\boldsymbol{L}_{Z_{N}}^{'} \Big)^{T} \Big( \eta_{Z_{N}} - P\boldsymbol{L}_{Z_{N}}^{'} \Big) \\ &- P\boldsymbol{L}_{Z_{N}}^{'} \Big) \end{split}$$

$$\begin{split} \eta_E &= 1/2*ln(L_E/L_{E0}), \; \eta_\sigma = 1/2*ln(L_\sigma/L_{\sigma0}), \; \eta_{\delta_b} \\ &= 1/2*ln(L_{\delta_b}/L_{\delta_b0}), \; \eta_{Z_b} = 1/2*ln(L_{Z_b}/L_{Z_b0}) \end{split}$$

and  $\lambda_E$ ,  $\lambda_\sigma$ ,  $\lambda_{\delta_b}$ , and  $\lambda_{Z_{\rm N}}$  are the constraint coefficients for the unknown parameter to be estimated,  $L_{E0}$ ,  $L_{\sigma 0}$ ,  $L_{\delta_b 0}$ , and  $L_{Z_{\rm N} 0}$  indicate the initial model parameters.

## 3. Examples

## 3.1. Synthetic examples

To validate the feasibility of the proposed inversion strategy, a well-log data of the shale gas reservoir is used as true model parameters. Young's modulus E, Poisson's ratio  $\sigma$ , Thomsen's weakly anisotropic parameter  $\delta_{\rm b}$ , and the normal excess compliance  $Z_{\rm N}$  can be calculated by the shale equivalent rock-physics model in Fig. 4. Based on the convolution model, a 35 Hz Ricker wavelet is used to generate synthetic seismic gathers at different incidence and

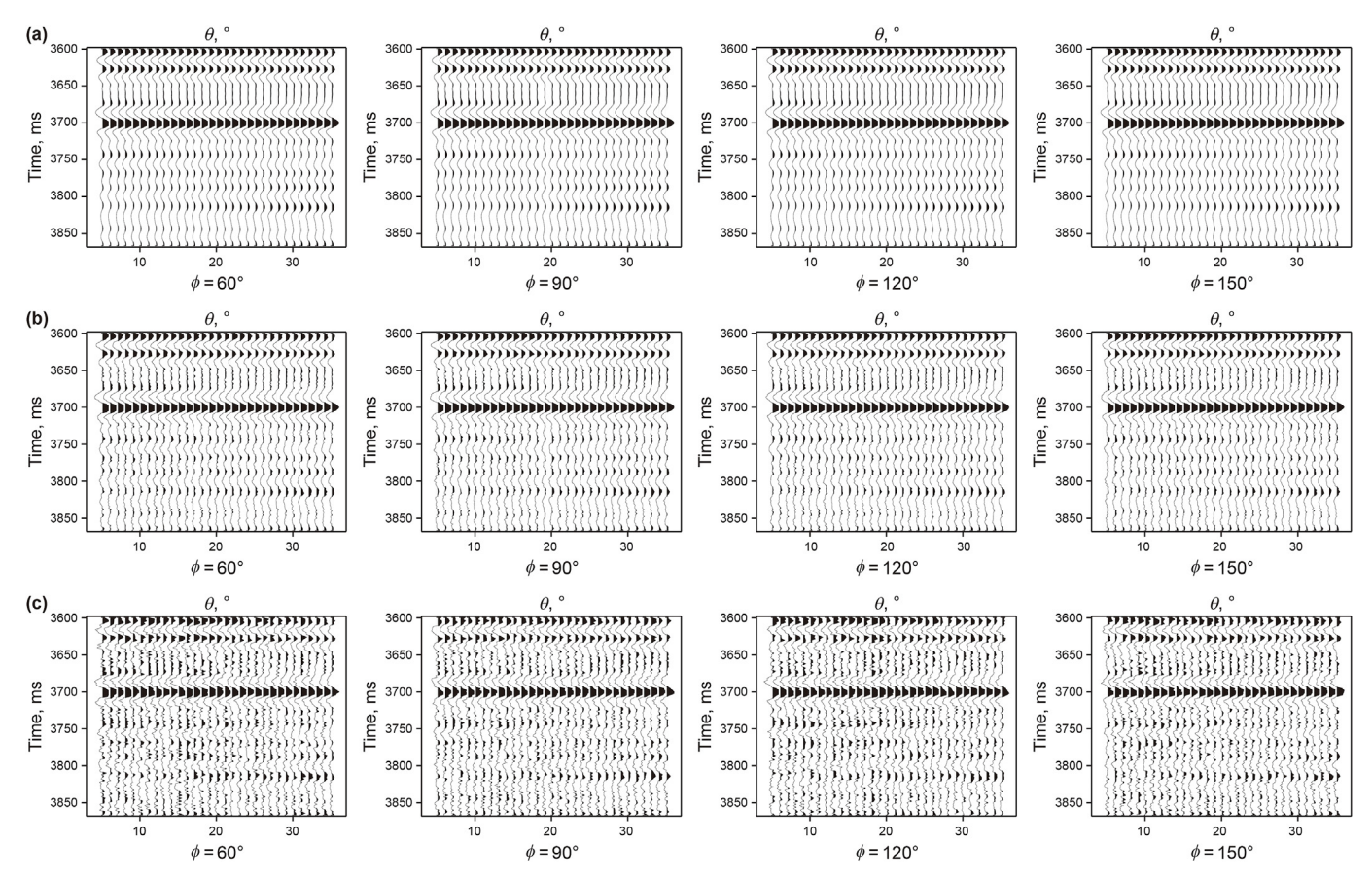


Fig. 5. Synthetic seismic angle gathers, in which (a) represents the case of noise-free, (b) represents the case of SNR = 5, (c) represents the case of SNR = 2.

azimuthal angles in Fig. 5. Azimuths are 60°, 90°, 120°, and 150°, and incidence angles range from  $0^{\circ}$  to  $30^{\circ}$ . Then we perform the Bayesian EI inversion for four model parameters, as shown in Figs. 6–11. In the case of noise-free synthetic seismic gathers being employed in the inversion, comparisons between the initial models (in green), the true values (in blue), and inverted results (in red) of Young's modulus E, Poisson's ratio  $\sigma$ , Thomsen's WA parameter  $\delta_{\rm b}$ , and the normal excess compliance  $Z_N$  are displayed in Fig. 6. To validate the accuracy of the inversion results with no noise in seismic data, we show the relative prediction errors of model parameters which is the difference between true values and inversion results divided by true values in Fig. 7. We observe the errors of Young's modulus E, Poisson's ratio  $\sigma$  are about within 4%, the errors of Thomsen's WA parameter  $\delta_{\rm h}$  and the normal excess compliance  $Z_{\rm N}$  are about within 20%, which illustrates the parameters can be estimated reasonably. Considering to add Gaussian noise into the synthetic seismic gathers, we generate the synthetic seismic traces with different signal-to-noise-ratios (SNR) to further examine the stability and robustness of the inversion workflow. In Figs. 8 and 10, we show the comparison between the real and estimated E,  $\sigma$ ,  $\delta_b$ , and  $Z_N$  for the case of SNR of 5 and 2, respectively. In Figs. 9 and 11, we can also see that the relative errors of Young's modulus E, Poisson's ratio  $\sigma$  are controlled within 5%, and the relative errors of fracture parameters are controlled within 30% even in the case of noise. The inversion results still have a high degree of agreement with the well log data, even though adding Gaussian random noise. Therefore, tests on synthetic seismic data demonstrate the feasibility and robustness of our new inversion approach.

# 3.2. Field data example

In order to demonstrate the stability and effectiveness of this new stress indicator, a field-data example of prestack seismic angle gathers is utilized to implement the Bayesian EI inversion. The seismic data of incidence angles of  $5^{\circ}$  (stacked over  $0^{\circ}-10^{\circ}$ ),  $15^{\circ}$  (stacked over  $10^{\circ}-20^{\circ}$ ), and  $25^{\circ}$  (stacked over  $20^{\circ}-30^{\circ}$ ), and the azimuths of  $60^{\circ}$  (stacked over  $30^{\circ}-90^{\circ}$ ),  $90^{\circ}$  (stacked over  $60^{\circ}-120^{\circ}$ ),  $120^{\circ}$  (stacked over  $90^{\circ}-150^{\circ}$ ), and  $150^{\circ}$  (stacked over  $120^{\circ}-180^{\circ}$ ) are utilized as the input datasets.

Real data acquired is situated in the Sichuan Basin, Southwest of China. The lithology is mostly black shale which contains brittle minerals of quartz, feldspar, and carbonate. The reservoir zone is situated at the bottom of the Longmaxi Formation and is rich in biosilica with a content ranging from 60% to 70%. The average value of the total organic carbon (TOC) content which is an important indicator for the hydrocarbon potential of shale reservoirs is 3.9%. The average total porosity is about 5.1%. The average gas saturation is 65%. Fig. 12 shows the results of the formation microimager (FMI) and fracture dip information of the different layers from well A. From Fig. 12, we can see that in a burial depth of 3530—3582 m, the Longmaxi Formation is a high-quality reservoir with plenty of vertical or near-vertical fractures and a small number of horizontal fractures developed. Therefore, we assume this gas-bearing shale reservoirs to be orthorhombic media.

First, we use the azimuthal angle gathers with four azimuths to perform the Bayesian El inversion. Fig. 13 shows the corresponding azimuthal El inversion results with three incidence angles and four

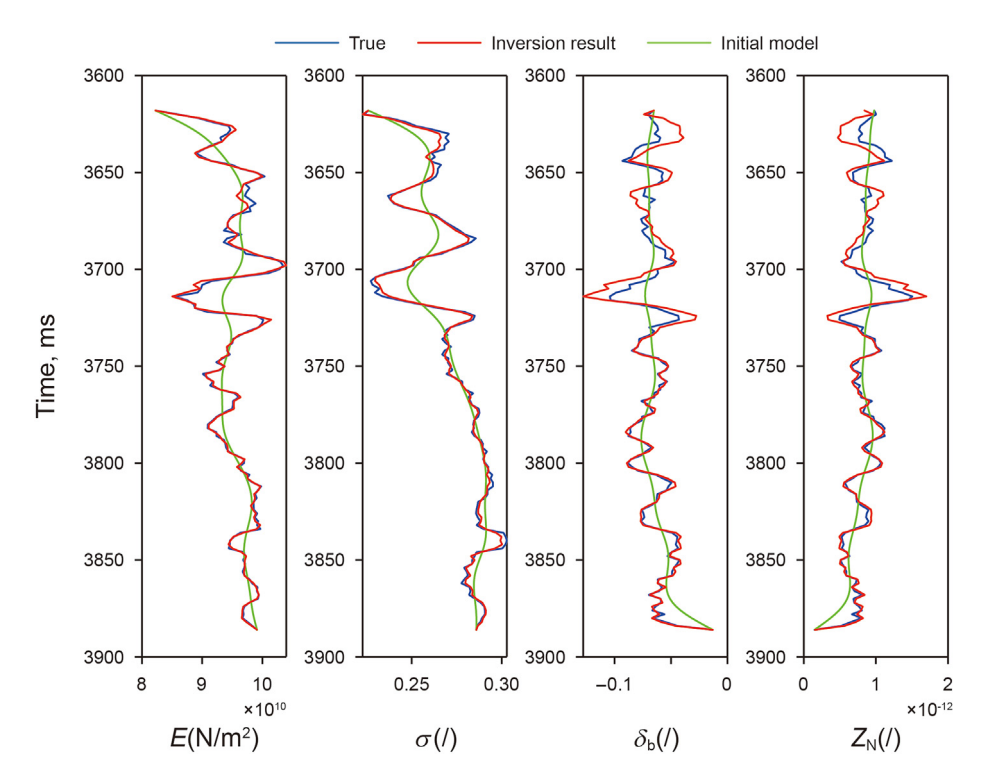


Fig. 6. Comparisons between inversion results (red), initial model values (green), and true values (blue) of the model parameters without noise.

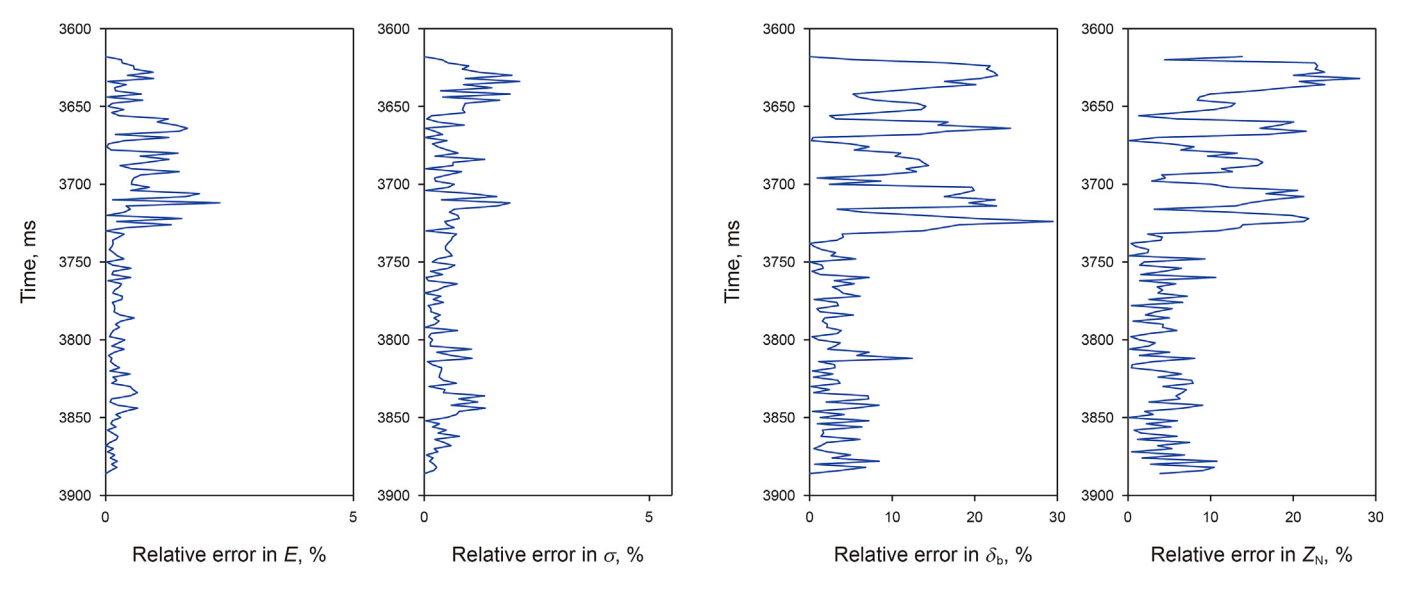


Fig. 7. Relative errors of the predicted model parameters without noise.

azimuths, in which (a) represents the estimated EI datasets with four different azimuths ( $60^{\circ}$ ,  $90^{\circ}$ ,  $120^{\circ}$ , and  $150^{\circ}$ ) at small incidence angle of  $5^{\circ}$ , (b) represents the estimated EI datasets at middle incidence angle of  $15^{\circ}$ , and (c) represents the estimated EI datasets at large incidence angle of  $25^{\circ}$ . In Fig. 13, the red lines point out the position of well log, and the white ellipses indicate the location of target reservoirs. EI inversion results show relatively low values in the vicinity of the shale reservoir.

We use the estimated azimuthal EI datasets to estimate Young's modulus E, Poisson's ratio  $\sigma$ , Thomsen's WA parameter  $\delta_b$ , and the normal excess compliance  $Z_{\rm N}$ , as shown in Fig. 14 and Fig. 15.

Figs. 14 and 15 show that the gas-bearing shale reservoir in the well is in the white ellipse area, which is within the time window from 1923 to 1945 ms. We observe that the inverted Young's modulus and Poisson's ratio exhibit relatively low values, while fracture parameters exhibit anomalously high values in the target area of the shale reservoir. Meanwhile, they all match the well log information, and the estimated profiles have fine continuity, which are consistent with the previous geology knowledge. Finally, the stress indicator  $ODHSR_{new}$  is predicted utilizing the estimated unknown parameters. Fig. 16 shows the inversion result of  $ODHSR_{new}$ , and the high values marked by the white ellipse in the profile represent the

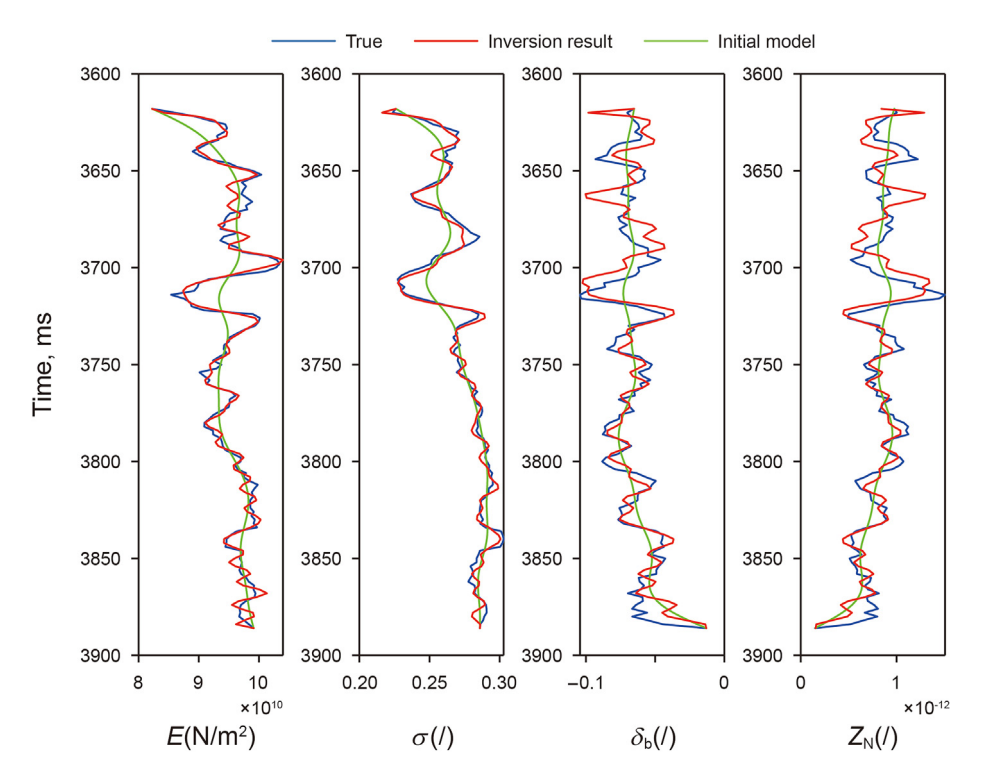


Fig. 8. Comparisons between inversion results (red), initial model values (green), and true values (blue) of the model parameters with SNR = 5.

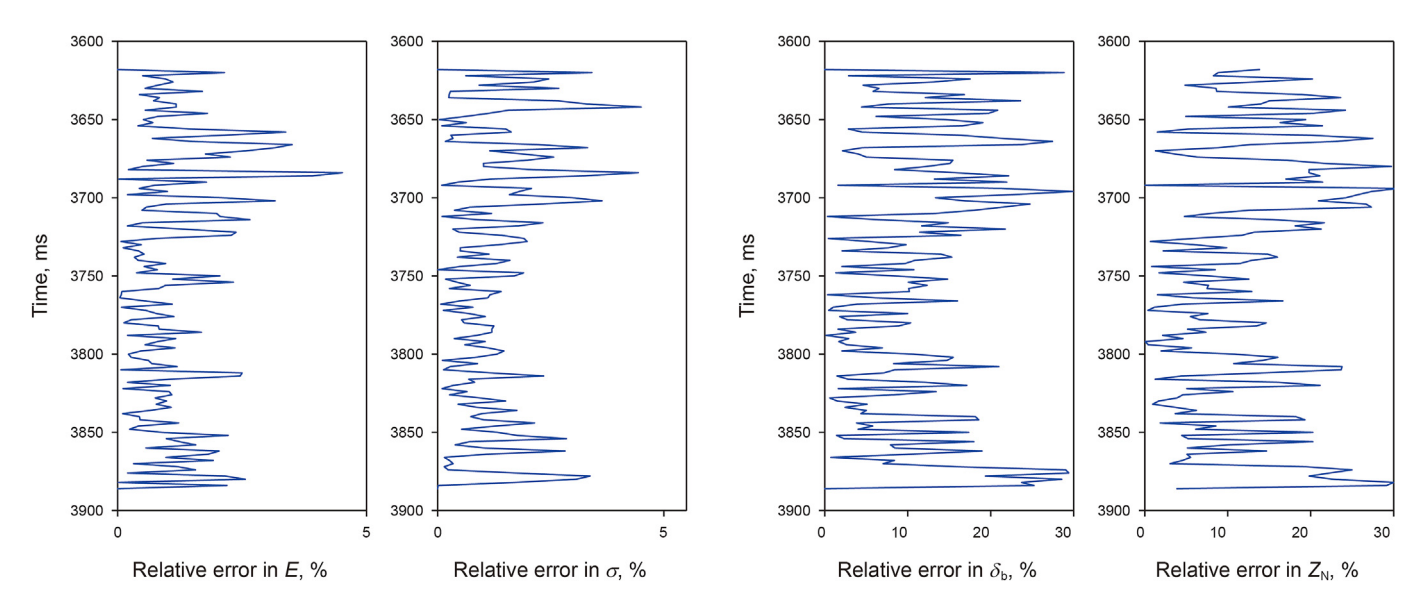


Fig. 9. Relative errors of the predicted model parameters with SNR = 5.

placements most likely to fracture into networks. Fig. 17 shows the comparisons between inversion results (red) and the smooth results of well logs (blue) at the well location. From Figs. 16 and 17, we observe there is a good match between the inversion result and the well-log data. The anomalously high *ODHSR*<sub>new</sub> areas in white ellipse indicate that there exist a variety of natural micro-fracture in the gas-saturated shale reservoir, and have the potential to develop multidirectional fractures for hydrocarbon migration and accumulation.

To further examine the reliability of the proposed approach, we provide a comparison analysis between the proposed approach and

the previous one. In Fig. 18, we show the estimated result of DHSR which is proposed by Gray (2002). The applicability of the previous stress indicator is restricted to the assumption of isotropic media and HTI media. The novel stress indicator *ODHSR*<sub>new</sub>, constructed based on the orthorhombic medium, have a more accurate identification of the stress state in actual shale reservoirs. Compared Fig. 18 with Fig. 16, we find that the lateral continuity of the inverted DHSR from the previous method is not as great as the novel stress indicator proposed, and the new stress indicator has a higher capability to describe stress characteristics than the conventional stress indicator in the target shale reservoir.

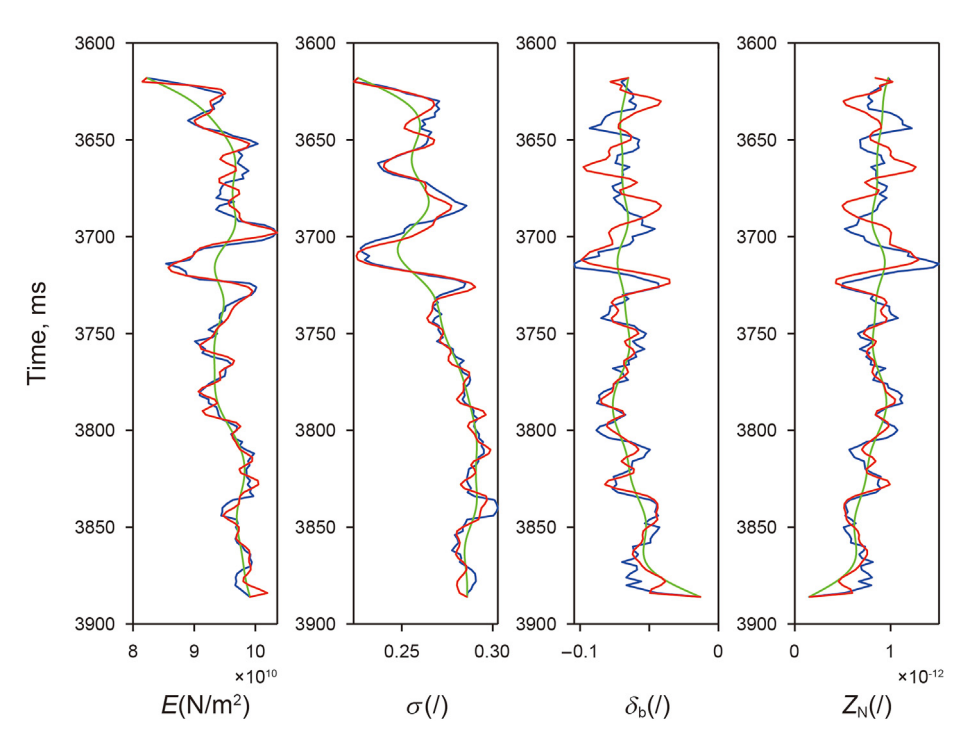
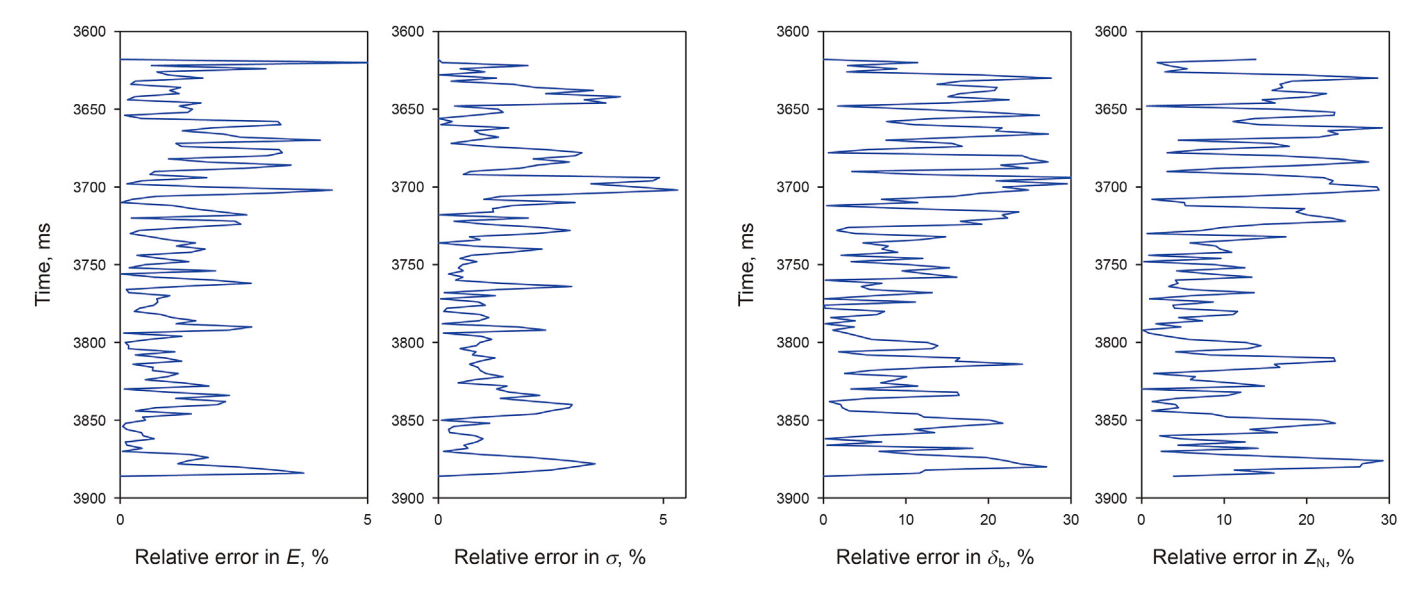


Fig. 10. Comparisons between inversion results (red), initial model values (green), and true values (blue) of the model parameters with SNR = 2.



**Fig. 11.** Relative errors of the predicted model parameters with SNR = 2.

### 4. Conclusions

The stress prediction is crucial for guiding the well location deployment and hydraulic fracturing of the gas-bearing shale reservoir. First, considering the complicated fractured shale formations in the field as a weakly orthorhombic medium, we construct a new stress indicator expressed by Young's modulus, Poisson's ratio, Thomsen's WA parameter and normal excess compliance for a weakly orthorhombic medium. Second, we derive and test a new simplified P-to-P reflection coefficient over a weakly orthorhombic medium that reduces the number of inverted parameters and enhances the robustness of the inversion. Based on

Bayesian azimuthal El inversion workflow, inversion tests on the synthetic examples show that rock mechanics parameters and fracture parameters can be reasonably estimated in a gas-bearing shale reservoir, and demonstrate the feasibility of the proposed new equation and the robustness of the inversion approach. Inversion tests on the field data examples reveal that the proposed inversion method is stable and reliable for parameter estimation, and the inverted results agree with well-log interpretation and geological prior information. Compared with the conventional method, the new approach effectively prevents the error accumulation and reduces the inversion multiplicity in stress evaluation. Finally, the distribution of stress indicator in the researched area

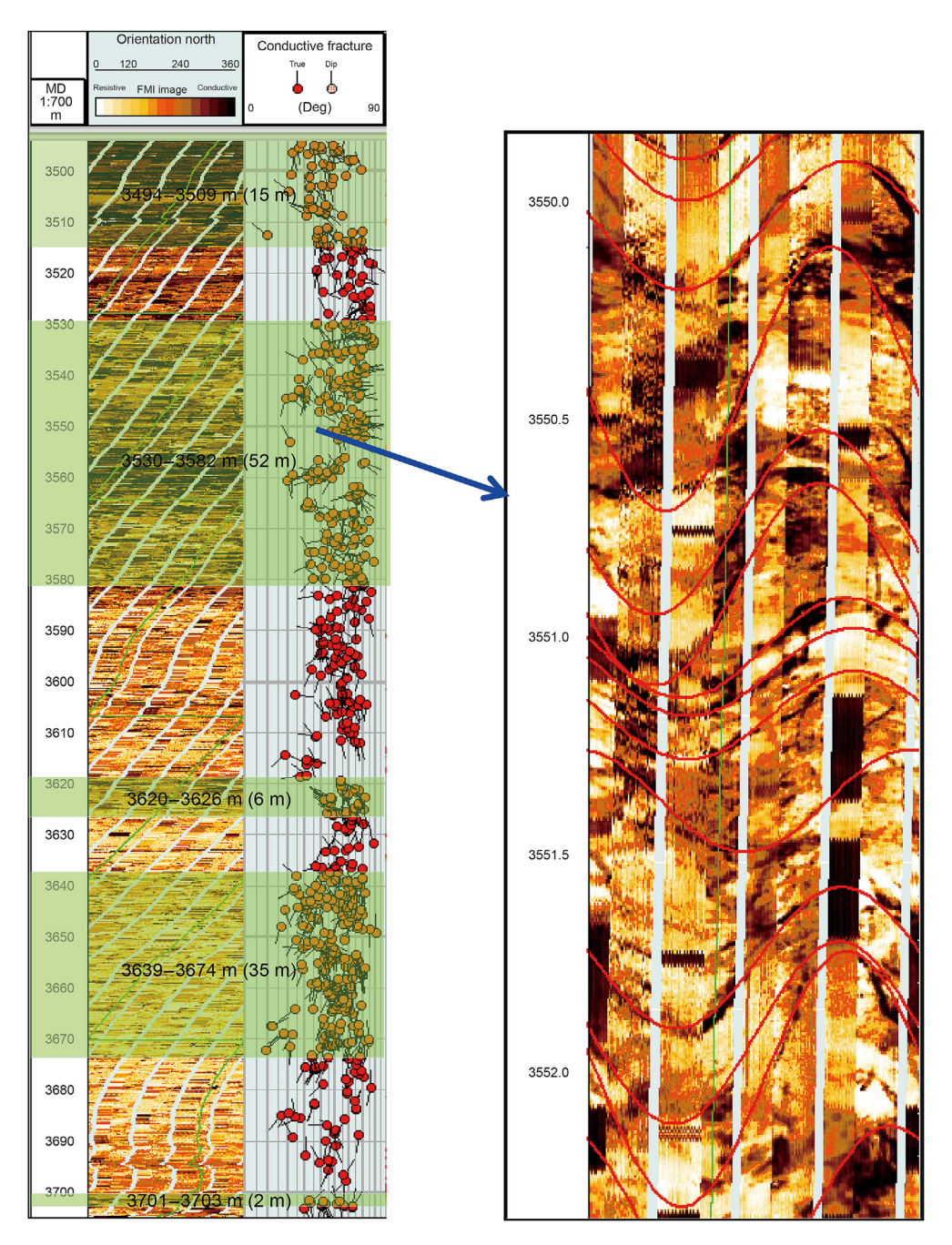


Fig. 12. FMI image logging picture of the vertical well A.

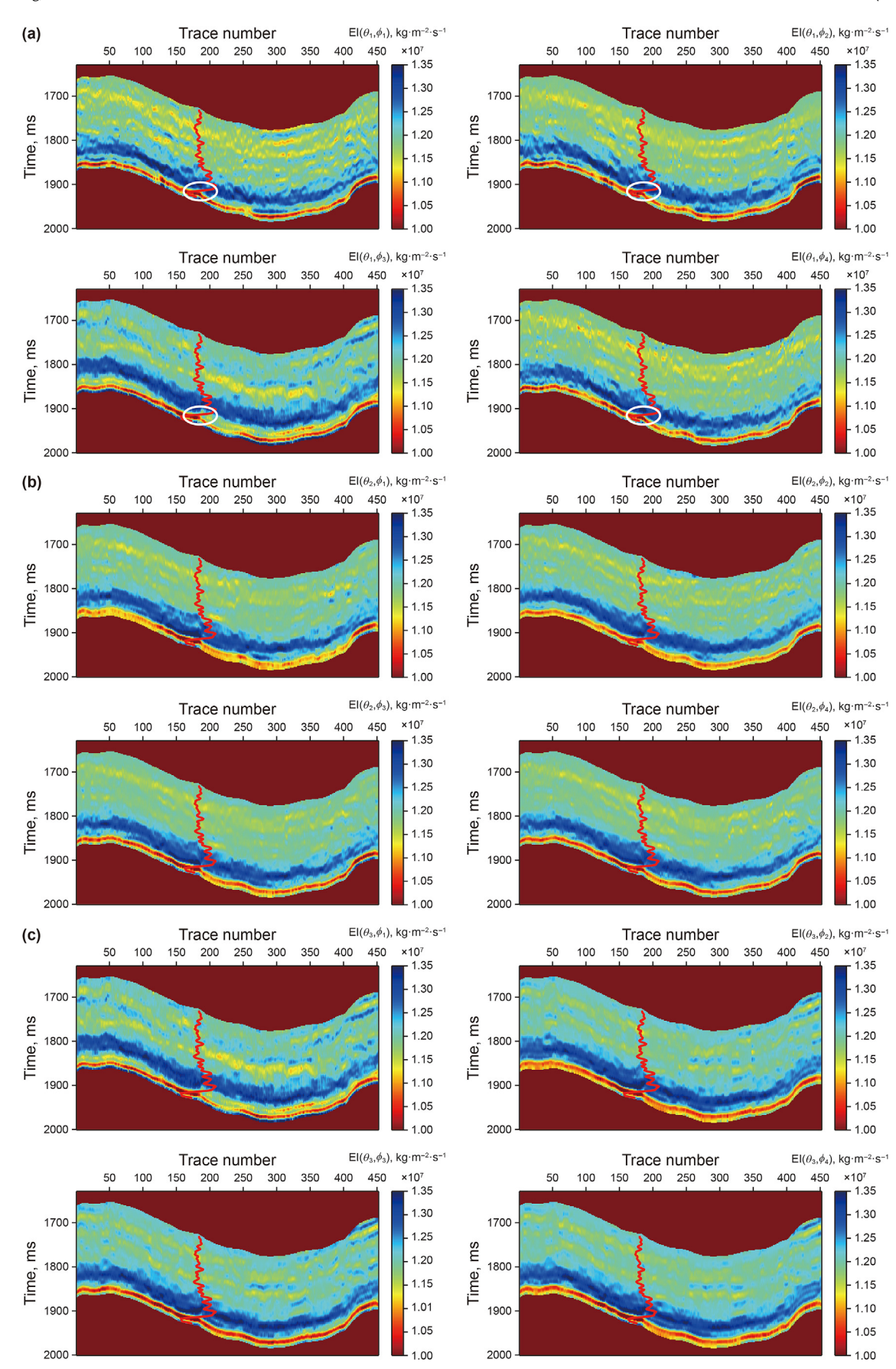


Fig. 13. (a) Shows inverted azimuthal EI at small incident angle of 5°, (b) shows inverted azimuthal EI at middle incident angle of 15°, and (c) shows inverted azimuthal EI at large incident angle of 25°. The red curve represents the well curve of EI data.

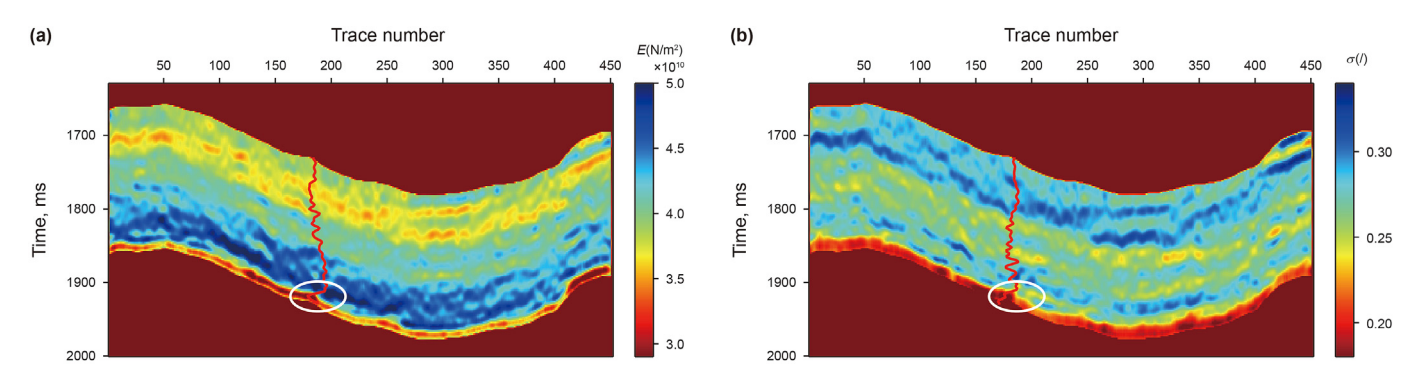
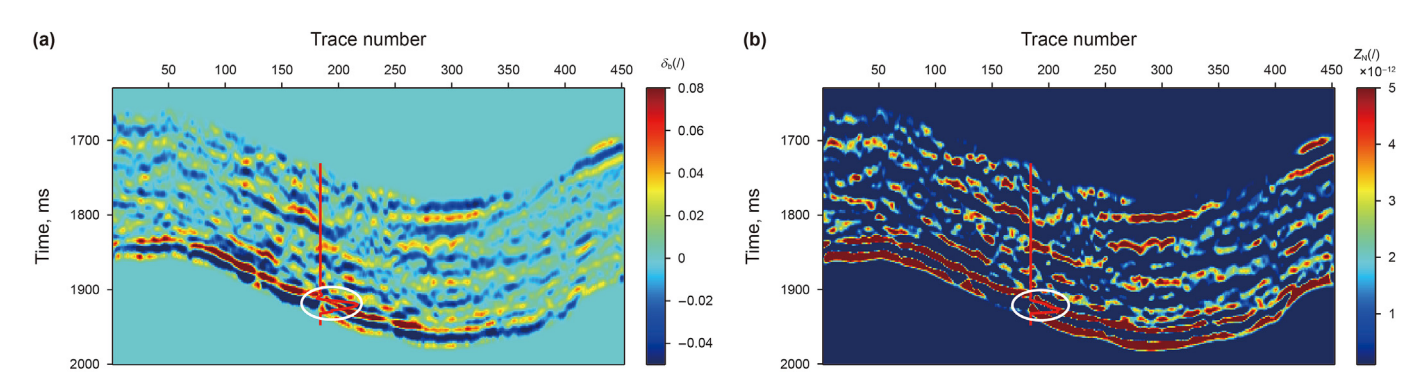


Fig. 14. (a) Shows the estimation of Young's modulus E from azimuthal El datasets, (b) shows the estimation of Poisson's ratio  $\sigma$  from azimuthal El datasets.



**Fig. 15.** (a) Shows the estimation of Thomsen's WA parameter  $\delta_b$  from azimuthal El datasets, (b) shows the estimation of normal excess compliance  $Z_N$  from azimuthal El datasets.

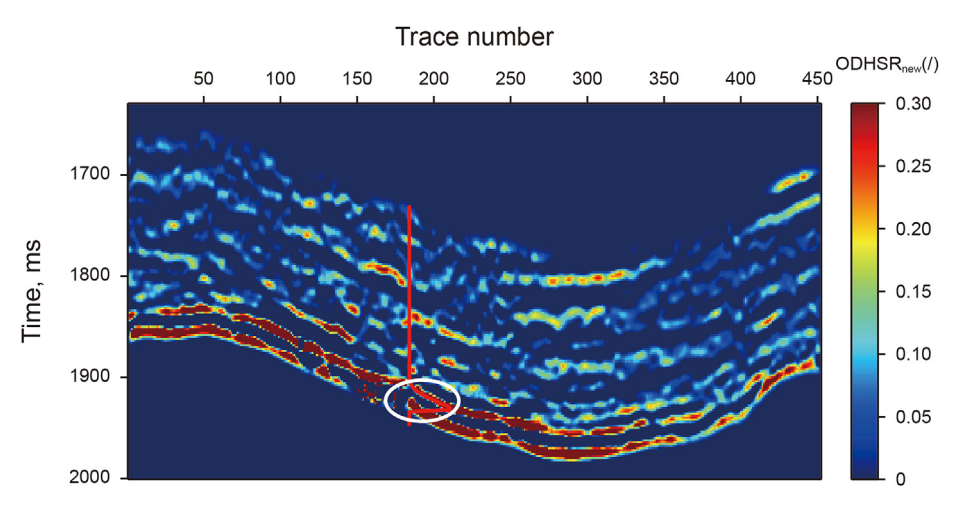


Fig. 16. Estimation of the stress indicator ODHSR<sub>new</sub> with proposed method in this study.

agrees well with the well information and can indicate the fracture developed zones. We conclude that the proposed stress indicator

can provide theoretical guidance for stress evaluation and fracturing reformation for the shale gas reservoir.

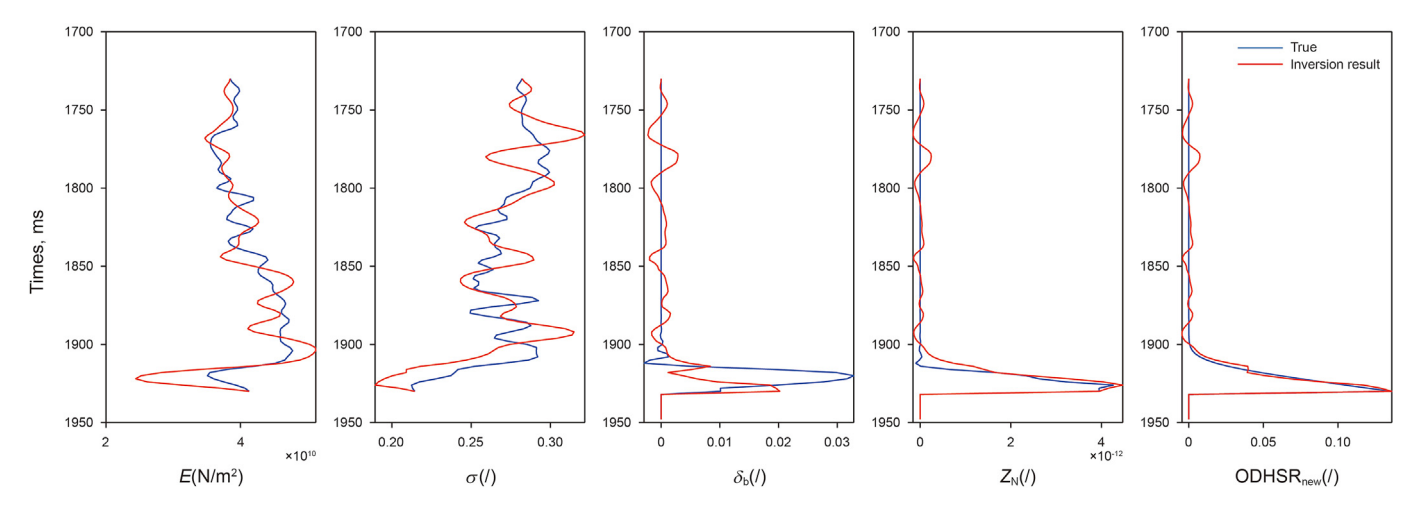


Fig. 17. Comparisons between inversion results (red) and the smooth results of well logs (blue) at the well location, where (a) shows the inverted Young's modulus, Poisson's ratio, Thomsen's WA parameter and normal excess compliance, (b) shows the inverted ODHSR<sub>new</sub>

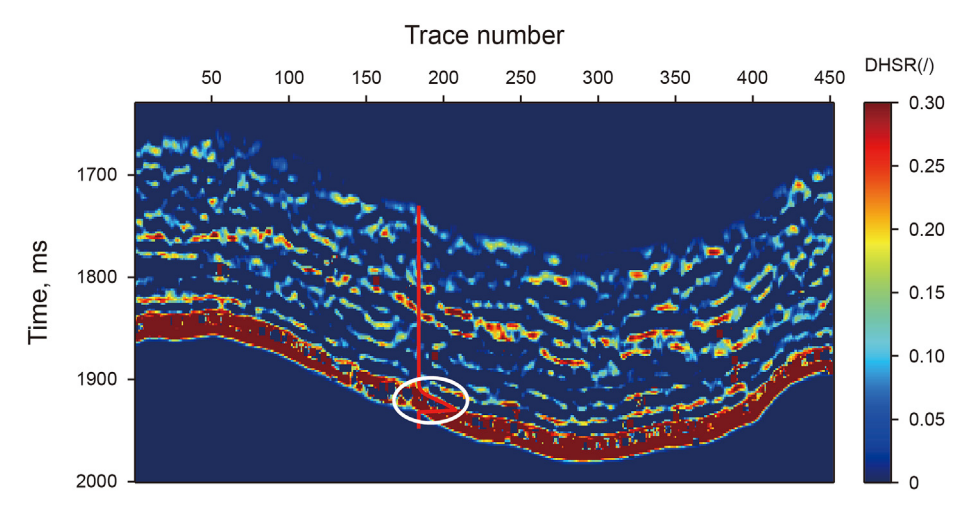


Fig. 18. Estimation of the stress indicator DHSR with conventional method.

### Acknowledgements

We would like to acknowledge the sponsorship of the National Natural Science Foundation of China (U19B2008, U19B6003, 42074136, 41674130), the National Oil and Gas Major Projects of China (2016ZX05027004-001), and PetroChina Prospective, Basic, and Strategic Technology Research Project (2021DJ0606).

### Appendix A

The elements in the compliance matrix in Eq. (1) are

$$s_{11} = \frac{c_{22}c_{33} - c_{23}^2}{c_{11}c_{22}c_{33} + 2c_{12}c_{23}c_{13} - c_{11}c_{23}^2 - c_{33}c_{12}^2 - c_{22}c_{13}^2} \quad \text{(A-1a)}$$

$$s_{12} = \frac{c_{23}c_{13} - c_{12}c_{33}}{c_{11}c_{22}c_{33} + 2c_{12}c_{23}c_{13} - c_{11}c_{23}^2 - c_{33}c_{12}^2 - c_{22}c_{13}^2}$$
 (A-1b)

$$s_{13} = \frac{c_{12}c_{23} - c_{22}c_{13}}{c_{11}c_{22}c_{33} + 2c_{12}c_{23}c_{13} - c_{11}c_{23}^2 - c_{33}c_{12}^2 - c_{22}c_{13}^2}$$
 (A-1c)

$$s_{22} = \frac{c_{11}c_{33} - c_{13}^2}{c_{11}c_{22}c_{33} + 2c_{12}c_{23}c_{13} - c_{11}c_{23}^2 - c_{33}c_{12}^2 - c_{22}c_{13}^2}$$
 (A-1d)

$$s_{23} = \frac{c_{12}c_{13} - c_{11}c_{23}}{c_{11}c_{22}c_{33} + 2c_{12}c_{23}c_{13} - c_{11}c_{23}^2 - c_{33}c_{12}^2 - c_{22}c_{13}^2}$$
 (A-1e)

$$s_{33} = \frac{c_{11}c_{22} - c_{12}^2}{c_{11}c_{22}c_{33} + 2c_{12}c_{23}c_{13} - c_{11}c_{23}^2 - c_{33}c_{12}^2 - c_{22}c_{13}^2}$$
 (A-1f)

$$s_{44} = \frac{1}{c_{44}} \tag{A-1g}$$

$$s_{55} = \frac{1}{c_{55}} \tag{A-1h}$$

$$s_{66} = \frac{1}{c_{66}} \tag{A-1i}$$

where, the stiffness components of the weakly orthorhombic media in Eqs. (A-1) presented by Pan et al. (2018b) are

$$\begin{split} C_{11} = & \frac{E(1-\sigma)}{(1+\sigma)(1-2\sigma)} - \frac{E^2(1-\sigma)^2}{(1+\sigma)^2(1-2\sigma)^2} Z_N \\ & + \frac{2E(1-\sigma)}{(1+\sigma)(1-2\sigma)} \varepsilon_b \end{split} \tag{A-2a}$$

$$\begin{split} C_{12} &= \frac{E\sigma}{(1+\sigma)(1-2\sigma)} - \frac{E^2\sigma(1-\sigma)}{(1+\sigma)^2(1-2\sigma)^2} Z_N \\ &\quad + \frac{2E(1-\sigma)}{(1+\sigma)(1-2\sigma)} \varepsilon_b - \frac{2E}{(1+\sigma)} \gamma_b \end{split} \tag{A-2b}$$

$$\begin{split} C_{13} &= \frac{E\sigma}{(1+\sigma)(1-2\sigma)} - \frac{E^2\sigma(1-\sigma)}{(1+\sigma)^2(1-2\sigma)^2} Z_N \\ &\quad + \frac{E(1-\sigma)}{(1+\sigma)(1-2\sigma)} \delta_b \end{split} \tag{A-2c}$$

$$\begin{split} C_{22} &= \frac{E(1-\sigma)}{(1+\sigma)(1-2\sigma)} - \frac{E^2\sigma^2}{(1+\sigma)^2(1-2\sigma)^2} Z_N \\ &\quad + \frac{2E(1-\sigma)}{(1+\sigma)(1-2\sigma)^2} \varepsilon_b \end{split} \tag{A-2d}$$

$$\begin{split} C_{23} &= \frac{E\sigma}{(1+\sigma)(1-2\sigma)} - \frac{E^2\sigma^2}{(1+\sigma)^2(1-2\sigma)^2} Z_N \\ &\quad + \frac{E(1-\sigma)}{(1+\sigma)(1-2\sigma)} \delta_b \end{split} \tag{A-2e}$$

$$C_{33} = \frac{E(1-\sigma)}{(1+\sigma)(1-2\sigma)} - \frac{E^2\sigma^2}{(1+\sigma)^2(1-2\sigma)^2} Z_N$$
 (A-2f)

$$C_{44} = \frac{E}{2(1+\sigma)} \tag{A-2g}$$

$$C_{55} = \frac{E}{2(1+\sigma)} - \frac{E^2}{4(1+\sigma)^2} Z_V$$
 (A-2h)

$$C_{66} = \frac{E}{2(1+\sigma)} - \frac{E^2}{4(1+\sigma)^2} Z_{H} - \frac{E}{(1+\sigma)} \gamma_{b}$$
 (A-2i)

where, E and  $\sigma$  represent Young's modulus and Poisson's ratio of homogeneous isotropic media, and  $\varepsilon_{\rm b}$ ,  $\gamma_{\rm b}$ ,  $\delta_{\rm b}$  represent Thomsen's weak anisotropic parameters of VTI background media, and  $Z_{\rm N}$ ,  $Z_{\rm V}$ , and  $Z_{\rm H}$  represent the normal, vertical and horizontal tangential excess compliances of vertical fractures.

### Appendix B

The covariance matrix of the reflection coefficients for unknown parameters is given by

$$\mathbf{C_r} = \begin{bmatrix} \sigma_{L_E}^2 & \sigma_{L_E L_\sigma} & \sigma_{L_E \delta_b} & \sigma_{L_E Z_N} \\ \sigma_{L_E L_\sigma} & \sigma_{L_\sigma}^2 & \sigma_{L_\sigma \delta_b} & \sigma_{L_\sigma Z_N} \\ \sigma_{L_E \delta_b} & \sigma_{L_\sigma \delta_b} & \sigma_{\delta_b}^2 & \sigma_{\delta_b Z_N} \\ \sigma_{L_E Z_N} & \sigma_{L_\sigma Z_N} & \sigma_{\delta_b Z_N} & \sigma_{Z_N}^2 \end{bmatrix}, \tag{B-1}$$

where  $\sigma_{L_E}^2$  is the variance of  $L_E$ , and  $\sigma_{L_E L_\sigma}$  is the covariance of  $L_E$  and  $L_\sigma$ .

The parameter covariance matrix  $C_r$  is decomposed as Eq. (28) based on the singular value decomposition (SVD) method (Downton 2005), which is given by

$$\mathbf{C_r} = \mathbf{u}\Lambda\mathbf{u}^{\mathbf{T}} = \mathbf{u} \begin{bmatrix} \sigma_1^2 & 0 & 0 & 0 \\ 0 & \sigma_2^2 & 0 & 0 \\ 0 & 0 & \sigma_3^2 & 0 \\ 0 & 0 & 0 & \sigma_4^2 \end{bmatrix} \mathbf{u}^{\mathbf{T}},$$
 (B-2)

where  $\mathbf{u}$  is the eigenvector and  $\mathbf{\Lambda}$  is the diagonal matrix of eigenvalues. The inverse of the eigenvector  $\mathbf{u}$  is given by

$$\mathbf{u}^{-1} = \begin{bmatrix} u_{11} & u_{12} & u_{13} & u_{14} \\ u_{21} & u_{22} & u_{23} & u_{24} \\ u_{31} & u_{32} & u_{33} & u_{34} \\ u_{41} & u_{42} & u_{43} & u_{44} \end{bmatrix}.$$
 (B-3)

In the case of J time sampling, the sparse covariance matrix of  $4J \times 4J$  is represented as

$$\mathbf{U}^{-1} = \begin{bmatrix} u_{11} & 0 & \dots & u_{12} & 0 & \dots & u_{13} & 0 & \dots & u_{14} & 0 & \dots \\ 0 & u_{11} & 0 & 0 & u_{12} & 0 & 0 & u_{13} & 0 & 0 & u_{14} & 0 \\ & & \dots & & & & & & & \\ u_{21} & 0 & \dots & u_{22} & 0 & \dots & u_{23} & 0 & \dots & u_{24} & 0 & \dots \\ 0 & u_{21} & 0 & 0 & u_{22} & 0 & 0 & u_{23} & 0 & 0 & u_{24} & 0 \\ & & \dots & & & & & & & \\ u_{31} & 0 & \dots & u_{32} & 0 & \dots & u_{33} & 0 & \dots & u_{34} & 0 & \dots \\ 0 & u_{31} & 0 & 0 & u_{32} & 0 & 0 & u_{33} & 0 & 0 & u_{34} & 0 \\ & & \dots & & & & & & & \\ u_{41} & 0 & \dots & u_{42} & 0 & \dots & u_{43} & 0 & \dots & u_{44} & 0 & \dots \end{bmatrix}_{4j \times 4j}$$

$$0 & u_{41} & 0 & 0 & u_{42} & 0 & 0 & u_{43} & 0 & 0 & u_{44} & 0 & \dots$$

We decorrelate the parameter matrixes for Eq. (26). The preconditioned coefficient matrix **G** and model matrix **m** are

$$\begin{cases} \mathbf{G}' = \mathbf{G}\mathbf{U} \\ \mathbf{m}' = \mathbf{U}^{-1}\mathbf{m} \end{cases}$$
 (B-5)

and

$$\mathbf{d} = \mathbf{G}'\mathbf{m}',\tag{B-6}$$

where  $\mathbf{G}'$  represents the coefficient matrix after decorrelation,  $\mathbf{U}$  represents the decorrelation matrix, and  $\mathbf{m}'$  represents the model parameter vector to be estimated after decorrelation.

### References

Bachrach, R., Sengupta, M., Salama, A., et al., 2009. Reconstruction of the layer anisotropic elastic parameters and high-resolution fracture characterization from P-wave data: a case study using seismic inversion and Bayesian rock physics parameter estimation. Geophys. Prospect. 57 (2), 253–262. https:// doi.org/10.1111/j.1365-2478.2008.00768.x.

Bachrach, R., 2015. Uncertainty and nonuniqueness in linearized AVAZ for orthorhombic media. Lead. Edge. 34 (9), 1048–1056. https://doi.org/10.1190/tle34091048.1

Bakulin, A., Grechka, V., Tsvankin, I., 2000. Estimation of fracture parameters from reflection seismic data—Part II: fractured models with orthorhombic symmetry. Geophysics. 65 (6), 1803—1817. https://doi.org/10.1190/1.1444864.

Bakulin, A., Grechka, V., Tsvankin, I., 2002. Seismic inversion for the parameters of two orthogonal fracture sets in a VTI background medium. Geophysics. 67 (1), 292–299. https://doi.org/10.1190/1.1451801.

Brew, S.R., 2012. Azimuthal Anisotropy Analysis to Determine Stress Regimes from a Reprocessed Full Azimuth 3D Seismic Survey. 74th EAGE Conference and Exhibition Incorporating EUROPEC 2012. European Association of Geoscientists & Engineers. https://doi.org/10.3997/2214-4609.20148170 cp-293-00073.

- Chen, H.Z., Li, J.X., Innanen, K.A., 2020. Nonlinear inversion of seismic amplitude variation with offset for an effective stress parameter. Geophysics 85 (4), R299–R311. https://doi.org/10.1190/geo2019-0154.1.
- Connolly, P., 1999. Elastic impedance. Lead. Edge. 18 (4), 438–452. https://doi.org/ 10.1190/1.1438307.
- Crampin, S., 2001. Developing stress-monitoring sites using cross-hole seismology to stress-forecast the times and magnitudes of future earthquakes. Tectonophysics. 338 (3–4), 233–245. https://doi.org/10.1016/S0040-1951(01)00079-8.
- Crampin, S., Gao, Y., 2006. A review of techniques for measuring shear-wave splitting above small earthquakes. Phys. Earth Planet. In. 159 (1–2), 1–14. https://doi.org/10.1016/j.pepi.2006.06.002.
- Du, B.Y., Yang, W.Y., Wang, E.L., et al., 2015. AVAZ inversion based on Young's modulus, Poisson's ratio and anisotropy gradient in fractured media. Geophys. Prospect. Pet. 4 (2), 218–225. https://doi.org/10.3969/j.issn.1000-1441.2015.02.014 (in Chinese).
- Du, B.Y., Zhang, G.Z., Zhang, J.J., et al., 2021. Stress prediction and evaluation approach based on azimuthal amplitude-versus-offset inversion of unconventional reservoirs. Geophys. Prospect. 69 (2), 372–387. https://doi.org/10.1111/ 1365-2478.13035.
- Gardner, G., Gardner, L., Gregory, A., 1974. Formation velocity and density-the diagnostic basics for stratigraphic traps. Geophysics. 39, 770–780. https:// doi.org/10.1190/1.1440465.
- Gray, F.D., Schmidt, D., Delbecq, F., 2010. Optimize shale gas field development using stresses and rock strength derived from 3D seismic data. In: Canadian Unconventional Resources and International Petroleum Conference. Society of Petroleum Engineers. https://doi.org/10.2118/137315-MS.
- Gray, F.D., Anderson, P., Logel, J., et al., 2012. Estimation of stress and geomechanical properties using 3D seismic data. First Break. 30 (3). https://doi.org/10.3997/1365-2397.2011042.
- Iverson, W.P., 1995. Closure stress calculations in anisotropic formations. In: SPE Low Permeability Reservoirs Symposium. Society of Petroleum Engineers. https://doi.org/10.2118/29598-MS.
- Ma, N., Yin, X.Y., Sun, C.Y., et al., 2017. The stress seismic prediction method based on the theory of orthorhombic anisotropic media. Chin. J. Geophys. 60 (12), 4766–4775. https://doi.org/10.6038/cjg20171218 (in Chinese).
- Ma, N., Yin, X.Y., Sun, C.Y., et al., 2018. Inversion for crustal stress based on azimuthal seismic data. Chin. J. Geophys. 61 (2), 697–706. https://doi.org/ 10.6038/cjg2018L0183 (in Chinese).
- Macbeth, B.J., Cattet, M.R.L., Obbard, M.E., et al., 2012. Evaluation of hair cortisol concentration as a biomarker of long-term stress in free-ranging polar bears. Wildl. Soc. Bull. 36 (4), 747–758. https://doi.org/10.1002/wsb.219.
- Mallick, S., 2001. AVO and elastic impedance. Lead. Edge 20 (10), 1094–1104. https://doi.org/10.1190/1.1487239.
- Martins, J.L., 2006. Elastic impedance in weakly anisotropic media. Geophysics 71 (3), D73–D83. https://doi.org/10.1190/1.2195448.

- Pan, X.P., Zhang, G.Z., Yin, X.Y., 2018a. Elastic impedance variation with angle and azimuth inversion for brittleness and fracture parameters in anisotropic elastic media. Surv. Geophys. 39, 965–992. https://doi.org/10.1007/s10712-018-9491-1
- Pan, X.P., Zhang, G.Z., Yin, X.Y., 2018b. Azimuthal seismic amplitude variation with offset and azimuth inversion in weakly anisotropic media with orthorhombic symmetry. Surv. Geophys. 39 (1), 99–123. https://doi.org/10.1007/s10712-017-9434-2.
- Price, N.J., Cosgrove, J.W., 1990. Analysis of Geological Structures. Cambridge University Press.
- Pšenčík, I., Martins, J.L., 2001. Properties of weak contrast PP reflection/transmission coefficients for weakly anisotropic elastic media. Studia Geophys. Geod. 45 (2), 176–199. https://doi.org/10.1023/A:1021868328668.
- Rickman, R., Mullen, M.J., Petre, J.E., et al., September 2008. A practical use of shale petrophysics for stimulation design Optimization: all shale plays are not clones of the barnett shale. In: Paper Presented at the SPE Annual Technical Conference and Exhibition. https://doi.org/10.2118/115258-MS. Denver, Colorado, USA.
- Rüger, A., 2002. Reflection Coefficients and Azimuthal AVO Analysis in Anisotropic Media. Society of Exploration Geophysicists. https://doi.org/10.1190/ 1.9781560801764.
- Sayers, C.M., 2004. Monitoring Production-Induced Stress Changes Using Seismic Waves. SEG Technical Program Expanded Abstracts 2004. Society of Exploration Geophysicists, pp. 2287–2290. https://doi.org/10.1190/1.1845217.
- Schoenberg, M., Helbig, K., 1997. Orthorhombic media: modeling elastic wave behavior in a vertically fractured earth. Geophysics 62 (6), 1954–1974. https://doi.org/10.1190/1.1444297.
- Sena, A., Castillo, G., Chesser, K., et al., 2011. Seismic reservoir characterization in resource shale plays: stress analysis and sweet spot discrimination. Lead. Edge 30 (7), 758–764. https://doi.org/10.1190/1.3609090.
- Starr, J., 2011. Closure Stress Gradient Estimation of the Marcellus Shale from Seismic Data. SEG Technical Program Expanded Abstracts 2011. Society of Exploration Geophysicists, pp. 1789–1793. https://doi.org/10.1190/1.3627552.
- Thomsen, L., 1986. Weak elastic anisotropy. Geophysics 51, 1954–1966. https://doi.org/10.1190/1.1442051.
- Warpinski, N.R., Smith, M.B., 1989. Rock mechanics and fracture geometry. Recent Adv. Hydraulic Fracturing 12, 57–80.
- Yin, X.Y., Zhang, S.X., Zhang, F., 2013. Two-term elastic impedance inversion and russell fluid factor direct estimation approach for deep reservoir fluid identification. Chin. J. Geophys. 56 (7), 2378–2390. https://doi.org/10.6038/ cig20130724 (in Chinese).
- Zhang, G.Z., Chen, J.J., Chen, H.Z., et al., 2015. Prediction for formation stress of shale based on rock physics equivalent model. Chin. J. Geophys. 58 (6), 2112–2122. https://doi.org/10.6038/cjg20150625 (in Chinese).
- Zoeppritz, K., Erdbebenwellen, U., 1919. On the reflection and propagation of seismic waves. Gottingen Nachricten der Konigl 2, 66–84.
- Zong, Z.Y., Yin, X.Y., Zhang, F., et al., 2012. Reflection coefficient equation and prestack seismic inversion with Young's modulus and Poisson ratio. Chin. J. Geophys. 55 (11), 3786–3794. https://doi.org/10.6038/j.issn.0001-5733.2012.11.025 (in Chinese).